The Astrophysical Journal Supplement Series, 269:12 (19pp), 2023 November https://doi.org/10.3847/1538-4365/acdd66

X-Ray Spectral Characterization of the Young Cygnus OB2 Population

E. Flaccomio[1], J. F. Albacete-Colombo[2], J. J. Drake[3], M. G. Guarcello[1], V. Kashyap[3], N. J. Wright[4], K. Briggs[5], B. Ercolano[6,7], M. McCollough[3], and S. Sciortino[1]
[1] INAF-Osservatorio Astronomico di Palermo Giuseppe S. Vaiana, Piazza del Parlamento 1, I-90134 Palermo, Italy; ettore.flaccomio@inaf.it
[2] Universidad de Rio Negro, Sede Atlántica—CONICET, Viedma CP8500, Argentina
[3] Smithsonian Astrophysical Observatory, 60 Garden St., Cambridge, MA 02138, USA
[4] Astrophysics Group, Keele University, Keele, ST5 5BG, UK
[5] Hamburger Sternwarte, Universität Hamburg, Gojenbergsweg 112, D-21029, Hamburg, Germany
[6] Universitäts-Sternwarte München, Scheinerstr. 1, D-81679 München, Germany
[7] Excellence Cluster Origin and Structure of the Universe, Boltzmannstr. 2, D-85748 Garching bei München, Germany
Received 2018 January 23; revised 2018 November 15; accepted 2018 November 15; published 2023 October 25

Abstract

We analyze the X-ray spectra of the ∼8000 sources detected in the Cygnus OB2 Chandra Legacy Survey (this focus issue), with the goals of characterizing the coronal plasma of the young low-mass stars in the region and estimating their intrinsic X-ray luminosities. We adopt two different strategies for X-ray sources for which more or less than 20 photons were detected. For the brighter sample we fit the spectra with absorbed isothermal models. In order to limit uncertainties, for most of the fainter Cygnus OB2 members in this sample we constrain the spectral parameters to characteristic ranges defined from the brightest stars. For X-ray sources with <20 net photons we adopt a conversion factor from detected photon flux to intrinsic flux. This was defined, building on the results for the previous sample, as a function of the 20% quantile of the detected photon energy distributions, which we prove to also correlate well with extinction. We then use the X-ray extinction from the spectral fits to constrain the ratio between optical and X-ray extinction toward Cyg OB2, finding it consistent with standard "Galactic" values, when properly accounting for systematics. Finally, we exploit the large number of sources to constrain the average coronal abundances of several elements, through two different ensemble analyses of the X-ray spectra of low-mass Cyg OB2 members. We find the pattern of abundances to be largely consistent with that derived for the young stellar coronae in the Orion Nebula Cluster.

Unified Astronomy Thesaurus concepts: Stellar activity (1580); Stellar coronae (305); Pre-main sequence stars (1290); T Tauri stars (1681); Stellar abundances (1577); X-ray stars (1823)

1. Introduction

The Cygnus OB2 association is one of the most massive groups of young stars in the galaxy, harboring hundreds of OB stars (e.g., Schulte 1956; Massey & Thompson 1991; Comerón et al. 2002; Hanson 2003; Kiminki et al. 2007; Wright et al. 2015b) and tens of thousands of lower-mass, pre-main-sequence (PMS) stars (e.g., Albacete Colombo et al. 2007; Drew et al. 2008; Vink et al. 2008; Wright & Drake 2009). Embedded within the wider Cygnus X giant molecular cloud (Schneider et al. 2006), the association is the dominant source of feedback for the region (Wright et al. 2012; Guarcello et al. 2023a). Its size and proximity make Cyg OB2 the best available environment to study the formation and evolution of large OB associations (Wright et al. 2014b, 2016), the properties of both low- and high-mass stars (e.g., Kiminki & Kobulnicky 2012; Rauw et al. 2015), and the evolution of protoplanetary disks (Guarcello et al. 2013).

The Chandra Cygnus OB2 Legacy Survey is designed to explore many of these issues by providing a wide-area and uniform census of both the high- and low-mass stars in Cyg OB2 and their X-ray properties. The survey is composed of a mosaic of overlapping Chandra ACIS-I pointings covering the central 1° area of the massive young stellar association Cyg OB2. The observations and resulting source catalog are described in Wright et al. (2023a), with an analysis of the sensitivity and completeness of the observations in Wright et al. (2023b). Guarcello et al. (2023b) correlate the X-ray catalog with available optical and infrared (IR) photometric catalogs, together with new deep optical photometry. Kashyap et al. (2023) exploit the X-ray and optical/IR information to assess the relation of the X-ray sources with the Cyg OB2 region. In short, ∼8000 X-ray point sources were detected, ∼6000 of which are associated with young members of the Cyg OB2 association. The remainder are associated with interloping field stars, mostly in the foreground, and with background extragalactic sources, mostly active galactic nuclei (AGNs).

Scientific motivation for studying the X-ray properties of Cyg OB2 stars falls into two broad categories. First, the association represents a slightly older group of PMS stars than has been studied in detail in similar large surveys, such as the Orion Nebula Cluster (ONC; Hillenbrand 1997; Getman et al. 2005). Stars in the ONC have been estimated to have an average age of about 2–3 Myr (Da Rio et al. 2010), whereas Wright et al. (2010) and Wright et al. (2015b) have found Cyg OB2 to have a mean age of about 5 Myr, but with an age spread of about 3–4 Myr. Stars in Cyg OB2 therefore represent an important large sample with which to assess how magnetic activity and X-ray emission evolve in the first few million years that are key to protoplanetary disk evolution and planet formation.

Second, basic X-ray spectral information is also used by Kashyap et al. (2023) for their membership analysis, exploiting the fact that the X-ray spectra of members, foreground sources, and background sources differ significantly, at least

statistically. The strong and hard X-ray emission of PMS stars with respect to that of older late-type stars (Feigelson et al. 2005) can be exploited to identify young stars and separate them from foreground stellar contaminants. Contamination from background AGNs can also be accounted for, at least in part, in a similar fashion, since AGNs will have harder X-ray emission spectra and be subject to even larger extinction with respect to members.

In this paper, we focus on the Chandra CCD-resolution X-ray spectra of low-mass ($\lesssim 2\ M_{\odot}$) Cyg OB2 members to characterize their X-ray-emitting plasma, characterize the X-ray extinction due to the intervening interstellar matter, and finally estimate their X-ray fluxes and luminosities. Most of our sources are detected with very few counts, and in our analysis we will take advantage of the results of Albacete-Colombo et al. (2023), who use Monte Carlo methods to perform a statistical assessment of the X-ray spectral fitting procedures in the low-count regime. We note that the bright spectra of O- and B-type stars, as well as the W-R stars in Cyg OB2, are discussed in more detail by Rauw et al. (2015).

This paper is organized as follows: Section 2 describes the X-ray data set, summarizes the source classification in terms of membership, and presents the average spectral features by source class. The spectral analysis and the methods employed are presented in Section 3. In Section 4 we present how the average abundances of some of the elements in the X-ray-emitting plasma were constrained, exploiting our large source sample. Section 5 discusses the implications of our results with regard to the properties of coronal plasma, coronal abundances, and the relation between X-ray and optical extinction toward our Cyg OB members. Finally, all the results are briefly summarized in Section 6.

2. Data and Sample Selection

Our starting point is the X-ray source catalog and photon extraction products obtained by Wright et al. (2023a) using the ACIS Extract analysis software (Broos et al. 2010). In short, using a variety of techniques suitable for the analysis of multiple, overlapping but nonaligned Chandra ACIS observations, source and background photon lists were obtained for each of the 7924 detected X-ray sources, along with appropriate instrumental response files. In the great majority of cases, photons for a given source were collected from several observations, each with a different effective exposure time, point-spread function (PSF), background, and spectral response. The ACIS Extract analysis merges all the *suitable* observations to produce a single average source (and background) spectrum with associated instrumental response.

We analyzed these time-averaged spectra for the full sample of 7924 sources. Most of our discussion will, however, be focused on low-mass Cyg OB2 members. The X-ray spectra of the 100 or so known massive, O and B and W-R stars in Cyg OB2 were also analyzed in the same way, but the reader is referred to Rauw et al. (2015) for a more in-depth analysis and discussion of their X-ray properties.[8] Excluding these high-mass stars, the number of extracted source photons in the 0.5–8.0 keV band, including the background contribution, ranges from 3 to 3870. In the following, we will also consider a subsample of bright X-ray sources, i.e., the 2805 sources found with >20 net (i.e., background-subtracted) counts, to which we will limit our spectral fitting analysis.

The background contribution within the source extraction regions can be significant for fainter sources, which are the great majority: for 33% of all sources (46% of sources with <20 net counts), background photons are more numerous than source photons. Only for 7.2% of the sources (2.0% of those with <20 counts) does the background contribute less than 10% of the net source counts. These large background contributions are partly due to the mapping strategy of the survey, which resulted in all sources being observed both close to on-axis, where the PSFs and extraction regions are small, and off-axis, where the PSFs, extraction regions, and hence background contributions are commensurately larger. The merged source and background photon lists and spectra provided by ACIS Extract are produced by merging the data from the available observations in such a way as to maximize the signal-to-noise ratio (S/N; see Broos et al. 2010 for details).

In the following, we will make use of optical and IR data for our X-ray sources. The cross-identification process and the adopted optical/IR catalogs are described by Guarcello et al. (2023b). When using optical/IR data, or derived quantities such as stellar masses, we will only consider the 5418 X-ray sources with a single optical/IR likely counterpart. These analyses will therefore exclude the 2423 X-ray sources (31%) with no plausible optical/IR counterpart and the 83 with more than one. However, when only sources with >20 counts are considered, just 10% are thereby excluded. We adopted the source classification from Kashyap et al. (2023), mostly based on a Bayesian analysis of optical, IR, and X-ray data. In particular, excluding sources with ambiguous optical/IR counterparts, the fractions of Cyg OB2 members, foreground sources, and background sources are 78%, 6%, and 16%, respectively (86%, 6%, and 8% for sources with >20 net counts).

2.1. Spectral Features by Source Class

Figure 1 shows the average X-ray spectra[9] for sources classified as low-mass Cyg OB2 members, foreground stars, and background objects with >20 net counts. As expected, foreground stars (mostly unabsorbed main-sequence coronal sources) have X-ray spectra that are softer than those of the young low-mass Cyg OB2 members (absorbed and hotter coronal sources), which are, in turn, significantly softer than those of background sources (even more absorbed and intrinsically harder AGNs with nonthermal spectra). These observations support the use of X-ray spectral characteristics for the assessment of membership, as performed by Kashyap et al. (2023).

Another, more quantitative way to show the difference between the three classes is to look at the quantiles of the energy distribution of detected photons, $Q_{X\%}$, where X is the fraction of source photons with energy $<Q_{X\%}$ (e.g., Hong et al. 2004). The actual calculation of quantiles and their relation with physical plasma parameters will be discussed in Section 3.3. Figure 2 shows, for sources with >20 net counts, the 75% quantile, $Q_{75\%}$, plotted against the 25% quantile, $Q_{25\%}$. Green, red, and blue symbols identify the low-mass members, foreground stars, and background stars, respectively,

[8] Four stars were not discussed by Rauw et al. (2015) because of strong pileup: CygOB2 #8a (cxo_id 4607), #5 (2197), #9 (4377), and #12 (2926). They are included in our analysis, but results are highly uncertain.

[9] The sum of all spectra divided by the total exposure time, computed with the COMBINE_SPECTRA tool in CIAO (Fruscione et al. 2006).

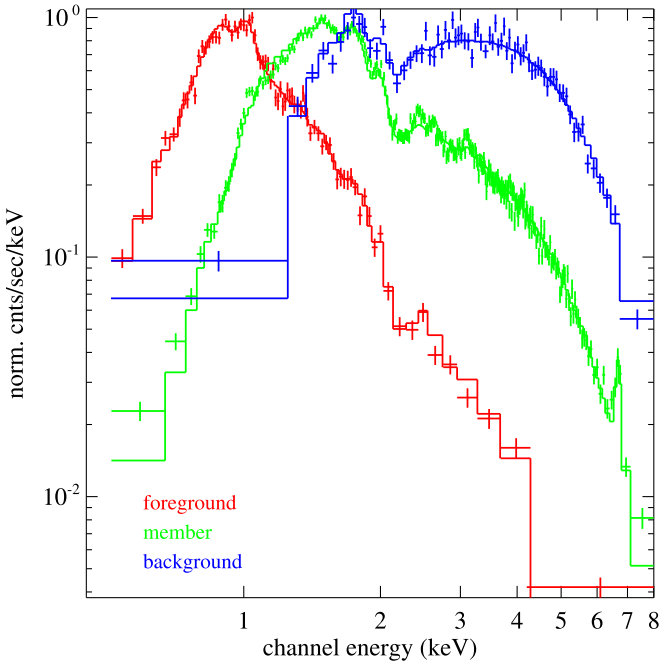

Figure 1. Average source spectra for X-ray sources detected with >20 net counts, associated with stars of different optical/IR/X-ray classes. The spectra of foreground stars and Cyg OB2 members, in red and green, respectively, are fitted here with absorbed isothermal models (TBABS × APEC). The average spectrum of background sources, in blue, is instead fitted with an absorbed power-law model (TBABS × POW).

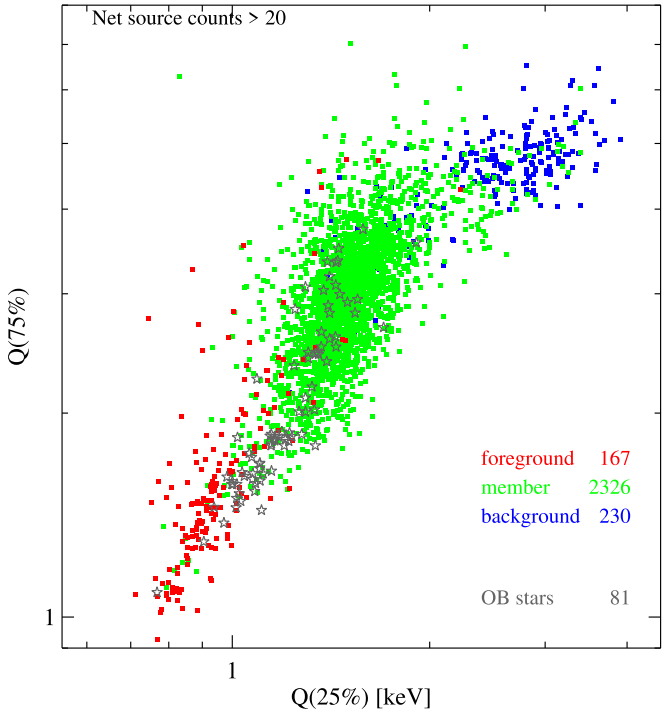

Figure 2. $Q_{75\%}$ vs. $Q_{25\%}$ for sources with >20 net counts. X-ray sources associated with Cyg OB2 low-mass members, foreground stars, and background stars are indicated by green, red, and blue squares, respectively. Gray star symbols indicate O- and B-type stars.

while O- and B-type stars, all presumed to be members of Cyg OB2, are plotted with gray star symbols. Clearly, $Q_{75\%}$ and, even more, $Q_{25\%}$ have different distributions for the three membership classes. As for the OB stars, some fall in the main body of the low-mass members, though a significant fraction have softer spectra, as expected for single O-type stars or systems with only one dominant supersonic wind source (Feldmeier et al. 1997; Rauw et al. 2015). The harder spectra may instead originate from the coronae of spatially unresolved low-mass companions, which, especially for late B-type stars, may dominate in X-rays, or from high-mass binaries or multiple systems in which two or more components have supersonic winds that collisionally interact.

3. Spectral Analysis

We here try to constrain the X-ray characteristics of the sources detected in our Chandra Cygnus OB2 survey, such as the temperature of the coronal plasma (for low-mass members of the region), the column density of the intervening absorbing gas, and the intrinsic absorption-corrected X-ray flux.

3.1. Methods

The low spectral resolution of ACIS-I pulse height spectra (∼150 eV at 1.5 keV[10]) and its complicated spectral response prevent the direct measurement of most intrinsic features (e.g., line and continuum fluxes) even for high-S/N spectra. Theoretical spectral models of emission and absorption, convolved through the instrumental response, must instead be fitted to the observed spectra in order to characterize the emission and line-of-sight absorption and to estimate intrinsic X-ray fluxes. For this purpose we have used the XSPEC package (Arnaud 1996) version 12.9 and the models provided therein. Specifically, we assume that the emission spectra can be described by the APEC or POW models, the former describing emission from isothermal optically thin plasma, as expected from stellar coronae, and the latter a simple power-law spectrum, as expected from extragalactic AGNs. These models were multiplied by the TBABS photoelectric absorption model to take into account absorption from interstellar and circumstellar material along the line of sight.

These models, with just one emission component, are the simplest possible for coronal and extragalactic sources, respectively. However, as we will see, they are adequate for the overwhelming majority of our sources. For Cyg OB2 members, this is at odds with results obtained for young stars in other regions, for which, when enough signal is available, two isothermal components are often required to provide an adequate fit to the emission from what is intrinsically a multitemperature plasma. This can likely be ascribed to two factors: (i) the higher-than-average extinction suffered by the stars in Cyg OB2 with respect to other regions (median $A_V = 5.4$ mag (Wright et al. 2023b), versus $\lesssim$1 mag for, e.g., the ONC or NGC 2264), effectively absorbing the lower-energy photons from the cooler thermal components, up to ∼1 keV (see Figure 1); and (ii) the low number of photons detected for most sources.

As noted above, we analyzed the X-ray spectra of all sources with >20 counts. The statistical uncertainties associated with such low numbers of counts imply rather large uncertainties on best-fit model parameters and X-ray fluxes. Care has been taken to estimate these uncertainties. Albacete-Colombo et al. (2023) provide a full discussion of how the uncertainties of best-fit parameters depend on the source photon counts,

[10] http://cxc.harvard.edu/proposer/POG

background, and spectral parameters. For the fainter Cyg OB2 members, we tried to limit the uncertainties on fluxes by constraining the spectral parameters $N_{\rm H}$ and kT to the rather limited ranges spanned by the brighter members.

For fainter sources, with <20 counts, the majority in our X-ray catalog, we adopted a simpler approach, discussed in Section 3.3, based on quantiles of the energies of detected photons.

3.2. Sources with >20 Counts

Prior to spectral fitting, we binned the spectra so that the first usable energy bin starts at 0.5 keV, the last ends at 8.0 keV, and each bin has an S/N $\gtrsim$ 1. Albacete-Colombo et al. (2023) found that this choice of S/N gives optimal results.[11] Since the S/N per bin depends on the background in that bin, this procedure results in bins with a variable number of source counts: depending on the source, the average bin contains between ∼3 and ∼120 photons (4.4 on average). The spectra for 30 sources, 27 of which are associated with members, turned out to have insufficient bins for useful spectral fits and were discarded from the fitting analysis.

Spectral fits of sources with >20 net detected counts were performed with the neutral hydrogen column density, $N_{\rm H}$, within the TBABS model, and the plasma temperature, kT, within the the VAPEC model, as free parameters. The same spectra were also fit with absorbed power-law models, allowing, again, the neutral hydrogen column density to vary together with the power-law slope, Γ, within the POW model. For both emission models, VAPEC and POW, the normalizations were kept fixed, since they were substituted, as free fit parameters, with the unabsorbed X-ray fluxes in the 0.5–8.0 keV band, $F_{\rm X}$, using the CFLUX convolution model. This has the advantage of allowing a straightforward estimation of uncertainties on best-fit unabsorbed flux values. The chemical abundances of the X-ray-emitting plasma were adopted from Maggio et al. (2007), derived from young stellar objects in the ONC, and were kept fixed in this stage of the fitting process.[12] This assumption will then be tested in Section 4, where we will derive *average* abundances largely consistent with Maggio et al. (2007). Furthermore, in view of the possible dependence of abundances on activity level and/or spectral type (see. Section 5.2), we checked that this choice, over that of a different and reasonable abundance set, has negligible effects on the estimated X-ray source flux, which is arguably the most important product of our spectral fitting, and small effects on $N_{\rm H}$ and kT (on average $<10^{21}$ cm^{-2} and <0.1 keV, respectively). We arrive at these conclusions in Appendix B comparing the isothermal fits with Maggio et al. (2007) abundances, described below, with similar fits using two very different and "extreme" abundance sets, i.e., those derived for V410 Tau and SU Aur by Telleschi et al. (2007b) with high-resolution X-ray spectra.

The Cash statistic (*C*-stat; Cash 1979) was adopted as the fit statistic, while the Pearson χ^2 was employed as a test statistic, i.e., to estimate, through the GOODNESS XSPEC command, how well the best-fit spectral model fits the data. Uncertainties (1σ) on our three parameters, $N_{\rm H}$, kT (or Γ), and $F_{\rm X}$, were obtained using the ERROR XSPEC command. In a very small number of cases, the calculation of uncertainties failed, although this is fortunately rarer for the flux than for the other two parameters. For the final choices of spectral models, upper and/or lower flux uncertainties are missing for only 11 sources, none of which were classified as a Cyg OB2 member.

Adopting absorbed isothermal models with unconstrained $N_{\rm H}$ and kT resulted in intrinsic flux estimates of low-count sources being very uncertain. For example, among the 531 low-mass members with 20–25 net counts, 54% (14%) have 1σ flux uncertainties larger than 0.3 (0.8) dex. This is mainly the result of the large (and correlated) uncertainties on $N_{\rm H}$ and kT. In order to establish reasonable flux estimates for ensuing studies, we have tried to reduce uncertainties by making reasonable assumptions on the range of true values for cluster members, based on the better-defined estimates obtained for the brightest sources.

Figure 3 shows the trends with source statistics of $N_{\rm H}$ and kT from unconstrained fits. Sources are color coded according to their member/foreground/background classification in Kashyap et al. (2023). Also shown are median error bars (1σ; green segments) and median parameter values and 1σ scatter (thicker crosses in orange), all computed, exclusively for members, in five different source count intervals. For both quantities, and in particular for $N_{\rm H}$, the uncertainties seem to explain much of the scatter among members, indicating (i) that the real ranges of $N_{\rm H}$ and kT spanned by members are probably rather small in comparison to the measurement error and (ii) that there is little evidence for a dependence of these ranges on source counts (or intensity). The great majority of low-mass members with high counts have $N_{\rm H}$ between 0.6×10^{22} cm^{-2} and 1.5×10^{22} cm^{-2}, with a median value, for all low-mass memers, of 0.95×10^{22} cm^{-2}. Likewise, the median kT of low-mass members is ∼2.9 keV. In this case, we may notice a shallow trend in the median kT with counts, consistent with previous reports indicating a direct relation between mean activity levels and plasma temperature (e.g., Preibisch et al. 2005b; Telleschi et al. 2007a). A high-kT tail is also apparent in the low-count bins, likely due to the hot plasma produced during magnetic flaring, and possibly more frequently at the faint luminosity end because of a detection bias. Following these considerations, it seems reasonable to assume that the characteristic temperature[13] of the vast majority of Cyg OB2 members ranges between 2.0 and 10.0 keV.

In order to try to limit the uncertainties on the intrinsic X-ray fluxes of Cyg OB2 members, while at the same time trying not to impose too strong a bias, we chose a preferred spectral model using the following procedure. We start by adopting the unconstrained 1T spectral fits. For members only, if the 1σ range of allowed fluxes is larger than 0.6 dex, i.e., if the one-tailed uncertainty is greater than a factor of ∼2, we then considered a 1T fit in which $N_{\rm H}$ is constrained between 0.6×10^{22} cm^{-2} and 1.5×10^{22} cm^{-2} (we will refer to this model as $1T_{\rm NH}$). We adopt the latter fit only if statistically acceptable ($P_{\rm null} > 1\%$ or larger than that of the current choice, i.e., the unconstrained 1T fit) and the associated 1σ range of fluxes is <0.6 dex (or <1/10 that of the unconstrained 1T fit). Finally, if the 1σ range of allowed fluxes is still larger than 0.6 dex, we considered the 1T fits in which, in addition to $N_{\rm H}$, constrained as above, we also constrained kT to lie between 2.0 and

[11] For the binning we used IDL and a suitable routine within the ACIS Extract analysis package (GROUP_BINS_TO_SNR) that computes the S/N per bin using Gehrels's formula for the uncertainties in source and background counts.

[12] The abundances for the absorption model were instead kept at the solar values listed by Anders & Grevesse (1989).

[13] That is, the temperature that best represents the absorbed spectrum as fit by an isothermal model.

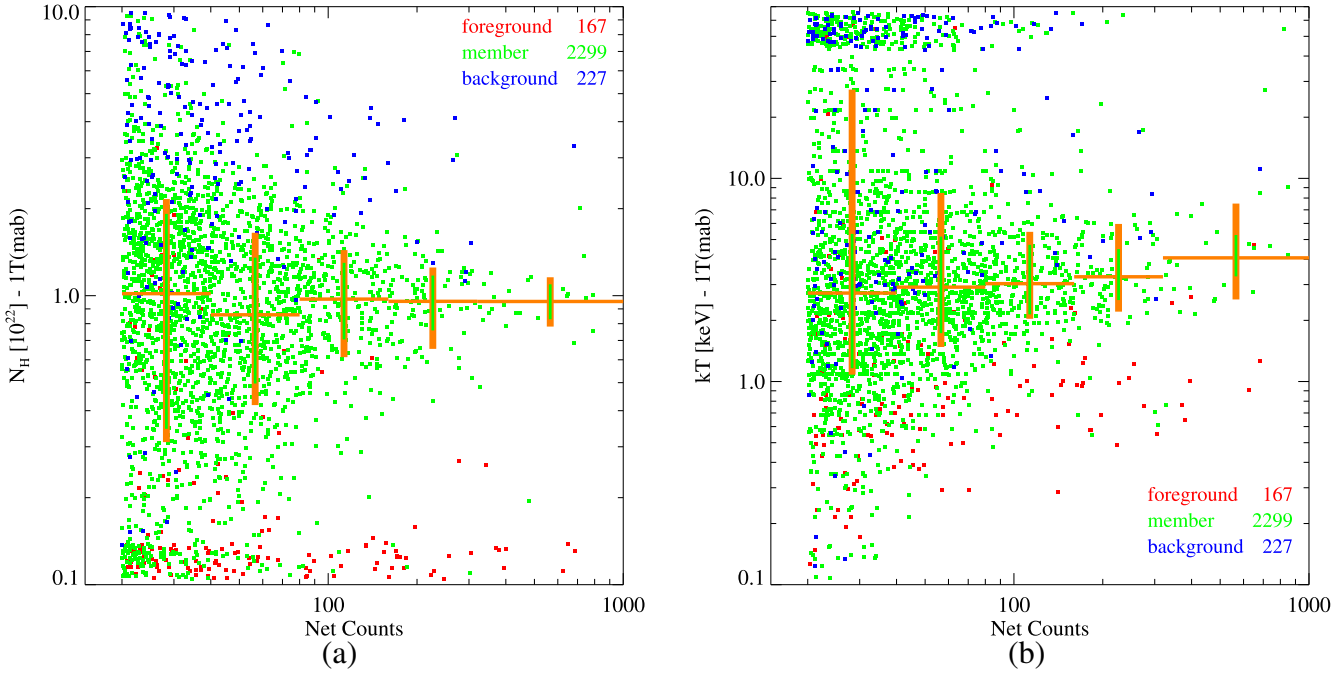

Figure 3. (a) Best-fit $N_{\rm H}$ from isothermal fits vs. source counts. X-ray sources are color coded according to their optical/IR class. Values beyond the plotting limits are plotted close to the respective axes, resulting in an artificial accumulation of points. The large orange crosses indicate the median and $\pm1\sigma$ quantiles of the distribution of $N_{\rm H}$ for members in selected ranges of net counts, marked by the horizontal bars. The lengths of the green bars within the thick orange ones represent the median of the upper and lower statistical uncertainties on $N_{\rm H}$ for the same samples. (b) Same as panel (a), but for the best-fit kT.

10.0 keV ($1T_{{\rm NH},kT}$). The latter fit was preferred to the current choice (1T or $1T_{\rm NH}$) only if statistically acceptable ($P_{\rm null} > 1\%$ or anyway larger than that of the current choice) and the associated 1σ range of fluxes was <0.6 dex wide (or <1/10 that of the current choice). As a last step, we examined by eye the X-ray spectra of sources associated with Cyg OB2 members and having the poorest spectral fits, as well as those for which the automatically assigned parameters were physically unreasonable (e.g., excessively low kT or very high fluxes). In 12 cases, new spectral models were assigned. In 11 of these cases, a second isothermal component was added to the emission model to improve the quality of the fit.

This procedure results in the adoption of $1{\rm T}/1T_{\rm NH}/1T_{{\rm NH},kT}$ fits for 70.8%/18.8%/9.3% of the 2362 low-mass members with >20 counts.[14] These fractions become 94.5%/4.4%/1.1% for the 840 low-mass members with >50 counts and 99.0%/0.7%/0.4% for the 287 low-mass members with >100 counts. In spite of this procedure, 2% of the low-mass members with >20 counts (and mostly <50 counts) remain with a 1σ flux range >0.6 dex.

Figure 4 shows the distributions of the final flux uncertainties (mean between upper and lower uncertainties) as a function of detected counts. The full results of our spectral fitting are reported in Table 1. Columns (1)–(3) list, for each X-ray source, the source identifier, the net counts detected in the 0.5–8.0 keV band, and the membership class from Kasyhap et al. (2018). Columns (4)–(7) indicate, for thermal model fits, the adopted emission model (i.e., whether one or two thermal components were needed, and whether $N_{\rm H}$ and kT were constrained), the null probability of the fit, and the values and uncertainties of the best-fit parameters: $N_{\rm H}$, kT (the emission-measure-weighted mean values for 2T models), and

[14] A fraction of 1.2% of these sources have no fits because the binned spectra have too few degrees of freedom.

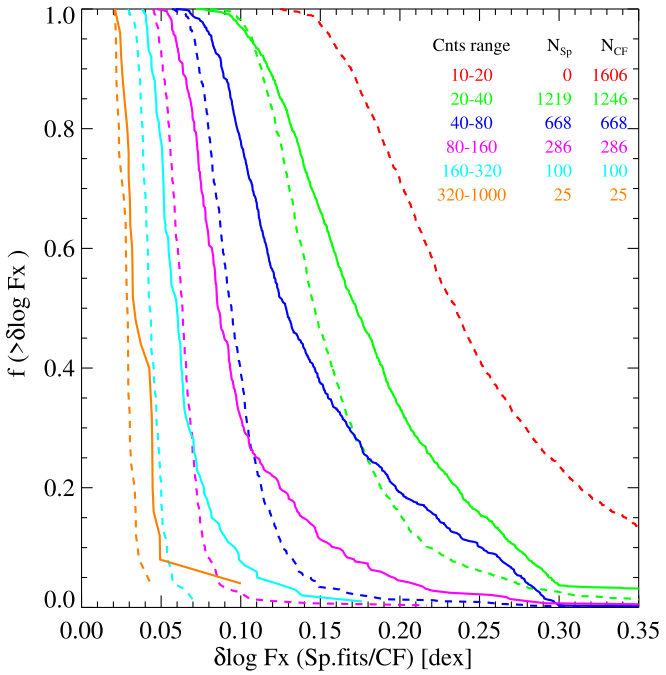

Figure 4. Cumulative distribution of uncertainties on the unabsorbed X-ray flux for *members* in different ranges of detected counts. Solid curves refer to uncertainties derived from spectral fits (Section 3.2). Dashed curves refer to the uncertainties on the fluxes derived using observed-to-intrinsic flux CFs (Section 3.3). In all cases the uncertainties are the mean of the upper and lower uncertainties. Count ranges and respective numbers of sources in the two samples are listed in the legend.

unabsorbed flux. As mentioned, we have also fitted all of our spectra with absorbed power laws, suitable for background AGNs. Unfortunately, our ACIS spectra are not adequate to distinguish between the intrinsic emission spectrum of a star and that of an AGN for the majority of sources, both because of

Table 1
Results of Spectral Fits and Quantile Analysis

Source			Isothermal Fit					Power-law Fit				Conversion Factor	
ID	Counts	Class	Model	Null Prob.	$N_{\rm H}$	kT	log Flux	Null Prob.	$N_{\rm H}$	Γ	log Flux	$Q_{20\%}$	log Flux
1	13.8	memb										1.61 ± 0.29	$-13.77^{0.21}_{0.21}$
2	24.9	memb	1T	59.9	$3.18^{2.73}_{1.35}$	$68.4_{63.5}$	$-13.29^{0.20}_{0.16}$	94.4	$0.97^{4.52}$	$-0.2^{1.5}_{0.9}$	$-13.37^{0.13}_{0.14}$	2.32 ± 0.58	$-13.21^{0.19}_{0.23}$
3	15.3	memb										2.12 ± 0.38	$-13.01^{0.19}_{0.19}$
4	23.2	bk	1T	43.7	$5.64^{4.30}_{2.14}$	$68.4_{64.0}$	$-13.17^{0.26}_{0.15}$	45.1	$2.84^{8.34}$	$-0.1^{1.7}_{1.2}$	$-13.33^{0.26}_{0.13}$	2.99 ± 0.69	$-13.08^{0.17}_{0.20}$
5	18.2	memb										1.51 ± 0.36	$-13.63^{0.21}_{0.24}$
6	22.5	bk	1T	97.6	$2.97^{2.69}_{1.16}$	$68.4_{64.7}$	$-13.35^{0.24}_{0.14}$	97.8	$3.19^{5.86}_{3.16}$	$0.8^{1.6}_{1.3}$	$-13.42^{0.48}_{0.15}$	2.39 ± 0.34	$-13.27^{0.15}_{0.15}$
7	4.4	memb										0.56 ± 0.19	$-14.85^{0.38}_{0.26}$
8	4.7	memb										1.07 ± 0.09	$-14.58^{0.35}_{0.25}$
9	9.6	fg										0.78 ± 0.12	$-14.41^{0.24}_{0.16}$
10	38.8	bk	1T	98.6	$4.47^{3.28}_{1.84}$	$2.8^{9.5}_{1.3}$	$-12.87^{0.44}_{0.24}$	96.9	$6.87^{6.68}_{3.43}$	$2.5^{1.7}_{1.2}$	$-12.72^{1.13}_{0.42}$	2.45 ± 0.31	$-12.97^{0.12}_{0.12}$
11	3.4	memb										0.71 ± 0.06	$-14.98^{0.43}_{0.28}$
12	8.3	bk										1.52 ± 0.29	$-13.99^{0.27}_{0.25}$
13	7.5	fg										0.95 ± 0.07	$-14.45^{0.25}_{0.19}$
14	12.3	memb										2.06 ± 0.39	$-13.63^{0.21}_{0.21}$
15	126.6	fg	1T	0.4	$0.21^{0.13}_{0.12}$	$1.0^{0.1}_{0.1}$	$-13.21^{0.13}_{0.12}$	0.4	$0.45^{0.19}_{0.17}$	$4.0^{0.6}_{0.5}$	$-12.85^{0.24}_{0.19}$	0.93 ± 0.02	$-13.27^{0.05}_{0.04}$
16	79.8	memb	1T	70.3	$6.84^{2.66}_{1.79}$	$13.7_{9.8}$	$-12.60^{0.21}_{0.12}$	72.9	$12.23^{5.93}_{4.30}$	$1.9^{1.0}_{0.8}$	$-12.47^{0.53}_{0.26}$	3.04 ± 0.13	$-12.59^{0.06}_{0.06}$
17	72.6	memb	1T	76.6	$1.24^{0.49}_{0.35}$	$22.7_{16.8}$	$-13.02^{0.08}_{0.07}$	77.5	$1.92^{0.88}_{0.74}$	$1.5^{0.5}_{0.5}$	$-13.01^{0.13}_{0.09}$	1.66 ± 0.13	$-13.02^{0.08}_{0.08}$
18	4.5	memb										1.40 ± 0.18	$-14.38^{0.36}_{0.25}$
19	9.5	memb										3.52 ± 0.63	$-13.36^{0.22}_{0.19}$
20	4.8	bk										2.58 ± 0.66	$-13.91^{0.36}_{0.30}$

their low S/N and because Cyg OB2 members have relatively hot coronae producing spectra that are more similar to power laws than those of cooler coronae. Results of the power-law fits are also reported in Table 1 (columns (8)–(11)). Table 2 provides the spectral parameters for the few X-ray sources needing a second thermal component.

Figure 5 shows $N_{\rm H}$ versus kT (average kT for two-temperature models), color coded according to our membership classification. The lowest $N_{\rm H}$ values and highest kT values, for which only upper and lower limits, respectively, can actually be constrained, are plotted as arrows corresponding to their 1σ limits.

3.3. Sources with <20 Counts

For sources with fewer than 20 detected counts, for which model fitting is impractical, we decided to adopt a different approach based on the spectral information summarized by chosen quantiles of the distribution of detected photon energies.

First, we computed, from the ACIS spectrum of each source, 11 quantiles, $Q_{X\%}$, where X, the fraction of source photons with energy $<Q_{X\%}$, ranges from 0.1 to 0.9 in steps of 0.1, and additionally included the values 0.25 and 0.75. The $Q_{X\%}$ values and their associated 1σ uncertainties, $\delta Q_{X\%}$, were estimated accounting for the background contribution to extracted source photons. To this end we followed Hong et al. (2004) and used their IDL routine (v1.7).

For similar intrinsic spectra, the quantiles are sensitive to the absorbing column density. The latter is, in turn, the main factor determining the reduction in flux from the intrinsic one at the source to the one observed at the detector (barring flux dilution due to distance, of course). We thus sought a relation between energy quantiles and the conversion factor (CF) needed to transform detected photon fluxes (in photons $\rm cm^{-2}\,s^{-1}$) into absorption-corrected energy fluxes (in erg $\rm cm^{-2}\,s^{-1}$).

We first investigated the sensitivity of each $Q_{X\%}$ to both of the X-ray spectral parameters, $N_{\rm H}$ and kT. In Figure 6(a) we plot, for example, $N_{\rm H}$ versus $Q_{20\%}$ for sources for which the 1σ uncertainty on the unabsorbed flux from spectral fits is <0.1 dex. Points are color coded according to optical/IR class. We find generally reasonable results: $N_{\rm H}$ correlates better with *low* quantiles, e.g., $Q_{10\%}$ or $Q_{20\%}$, while the quality of the correlation decreases as we move to *higher* quantiles. This is readily understood, as low quantiles are good proxies of the low-energy cutoff due to absorption. kT, on the other hand, correlates better with higher percentiles, although all quantiles saturate at high kT values. As for the CF, i.e., the ratio between detected photon flux and the absorption-corrected energy flux, as estimated through spectral fitting, Figure 6(b) shows the correlation with $Q_{20\%}$ (in the same sample as in Figure 6(a), i.e., sources with $\sigma(\log F_X) < 0.1$ dex). Disregarding O- and B-type stars (gray star symbols), a tight correlation is observed. In particular, for low-mass Cyg OB2 members, the 1σ y-axis dispersion of members around the quadratic best-fit correlation illustrated (solid gray line) is 0.044 dex, which is smaller than the median y-axis uncertainty of 0.075 dex for the points shown. Such dispersion about the mean relation is smaller than that obtained for the same stars using the median photon energy, $Q_{50\%}$: 0.063 dex.[15] We conclude that low quantiles are best suited to defining a relation with CF. This was not obvious a priori since, while we have seen that the relation with $N_{\rm H}$ is indeed better described by the low quantiles, the statistical

[15] Larger dispersions but consistent trends with percentiles are found when loosening the selection criterion on reliable flux values. Repeating the same correlation studies using all members with uncertainty on the unabsorbed flux from spectral fits <0.5 dex (instead of 0.1), we observe that the y-axis dispersions with respect to the mean relation for $Q_{20\%}$ and $Q_{50\%}$ are 0.142 and 0.163 dex, respectively.

Table 2
X-Ray Spectral Parameters for Two-temperature Fits

CXO ID	Counts	Class	Sp. Type	Null Prob.	N_H	$kT1$	$kT2$	norm1/norm2
797	1465.5	memb	O6IV+O9III	59.6	$1.27^{0.06}_{0.06}$	$0.59^{0.04}_{0.04}$	$5.4_{2.6}$	40.1
1168	1955.7	fg		45.0	$0.24^{0.05}_{0.05}$	$0.37^{0.02}_{0.02}$	$2.0^{0.3}_{0.2}$	2.3
2197[a]	20,978.5	memb	O7I+O6I+O9	0.0	$1.30^{0.02}_{0.02}$	$0.63^{0.02}_{0.02}$	$3.1^{0.3}_{0.2}$	8.6
2547	7474.3	memb	O7.5III	17.7	$1.55^{0.04}_{0.04}$	$0.74^{0.05}_{0.04}$	$3.0^{0.4}_{0.3}$	3.8
2926[a]	29,905.6	memb	B3.5Ia+	0.0	$1.80^{0.02}_{0.02}$	$0.71^{0.02}_{0.02}$	$2.9^{0.2}_{0.2}$	6.6
3895	3194.5	memb	O8II	27.8	$1.60^{0.05}_{0.05}$	$0.75^{0.06}_{0.05}$	$3.4^{2.0}_{0.7}$	11.6
4377[a]	15,863.8	memb	O5I+O3.5II	0.0	$1.50^{0.03}_{0.03}$	$0.64^{0.03}_{0.03}$	$6.1^{0.7}_{0.6}$	4.7
4607[a]	50,099.8	memb	O6I+O5.5II	0.0	$1.06^{0.02}_{0.02}$	$0.72^{0.02}_{0.02}$	$3.2^{0.1}_{0.1}$	2.1
5061	7353.7	memb	O5.5V	8.1	$1.26^{0.06}_{0.05}$	$0.68^{0.03}_{0.05}$	$2.6^{0.3}_{0.2}$	2.1
6534	522.0	fg		95.2	$0.00^{0.03}$	$0.84^{0.07}_{0.06}$	$3.5^{2.7}_{1.0}$	1.9
7883	1823.9	memb	WC6+O8III	3.5	$1.68^{0.12}_{0.13}$	$0.49^{0.08}_{0.07}$	$3.3^{0.6}_{0.5}$	8.8

Note.
[a] Sources whose X-ray spectra suffer from significant pileup. Spectral fits are statistically not acceptable, and best-fit parameters are uncertain.

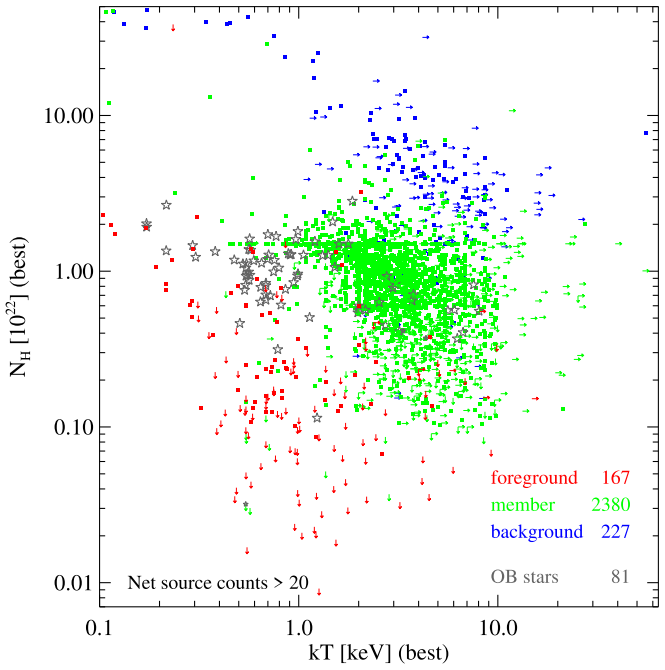

Figure 5. Final N_H vs. kT scatter plot. Symbols are color coded according to the optical/IR classification of sources, as noted in the legend. N_H values below the plotting limits and compatible with zero are plotted as upper limits at their upper 1σ uncertainty limit. Similarly, kT values with unconstrained upper bounds are plotted as lower limits at their lower 1σ limit.

uncertainties in their estimates are larger than those on quantile fractions closer to 50%.

We estimate unabsorbed fluxes from $Q_{20\%}$, the CFs derived from the quadratic fit in Figure 6(b) (limiting low values of $Q_{20\%}$ to 0.8, corresponding to ∼zero absorption), and the photon fluxes provided by ACIS Extract. Uncertainties on these fluxes were estimated propagating the uncertainties on $Q_{20\%}$ and those on the observed photon flux, taken to be of the same relative magnitude as the Poisson uncertainties on the observed counts.

Figure 7 shows, in different ranges of net source counts, the distributions of the differences between the fluxes obtained from the CFs and those obtained in Section 3.2 from spectral fittings. The median difference between the two estimates shows a small systematic offset, of order 0.01–0.02 dex, that is rather constant with source counting statistics. Differences can, however, become particularly severe and asymmetric at low counts, likely because of the significant uncertainties on the absorption correction obtained from spectral fitting, which sometimes leads to large and uncertain absorptions. Taking uncertainties into account, we indeed see that the two estimates are compatible within 1σ and 2σ for 90% and 98% of the low-mass members, respectively.

Distribution of the flux uncertainties as derived using CFs are shown in Figure 4 separately for stars in several count ranges (dashed curves) and compared with those from spectral fits (solid curves).

4. Coronal Abundances

Throughout our spectral analysis, we have consistently adopted the plasma abundances estimated by Maggio et al. (2007) for the brightest coronal sources in the ONC. These were obtained from ACIS CCD-resolution spectra obtained with the ∼850 ks Chandra Orion Ultradeep Project (COUP) observations. The spectra of a sample of 35 bright, high-S/N X-ray sources (>10,000 counts) were fit individually with the VAPEC model, i.e., the same optically thin thermal plasma emission model we have adopted here, but treating the abundances of individual elements as free fit parameters. Even with high S/N, CCD-resolution spectra only provide loose constraints on most abundances. For each element, Maggio et al. (2007) thus took the median values of the sample as representative of the true abundances.

We have attempted to estimate plasma abundances for our Cyg OB2 coronal sources, or at least verify that they are compatible with the assumed ones. With respect to the ONC case discussed by Maggio et al. (2007), our Cyg OB2 spectra have significantly lower S/N, and, because of the larger absorption of the region with respect to the ONC, they specifically lack signal at low energies, where the prominent lines of elements such as N and O are found. On the other hand, we can rely on a much larger stellar sample. For these reasons, instead of fitting individual spectra and taking the median abundances as in Maggio et al. (2007), we decided to investigate two alternative approaches.

Our first approach consists of fitting stacked spectra of large samples of Cyg OB2 members with either a single absorbed

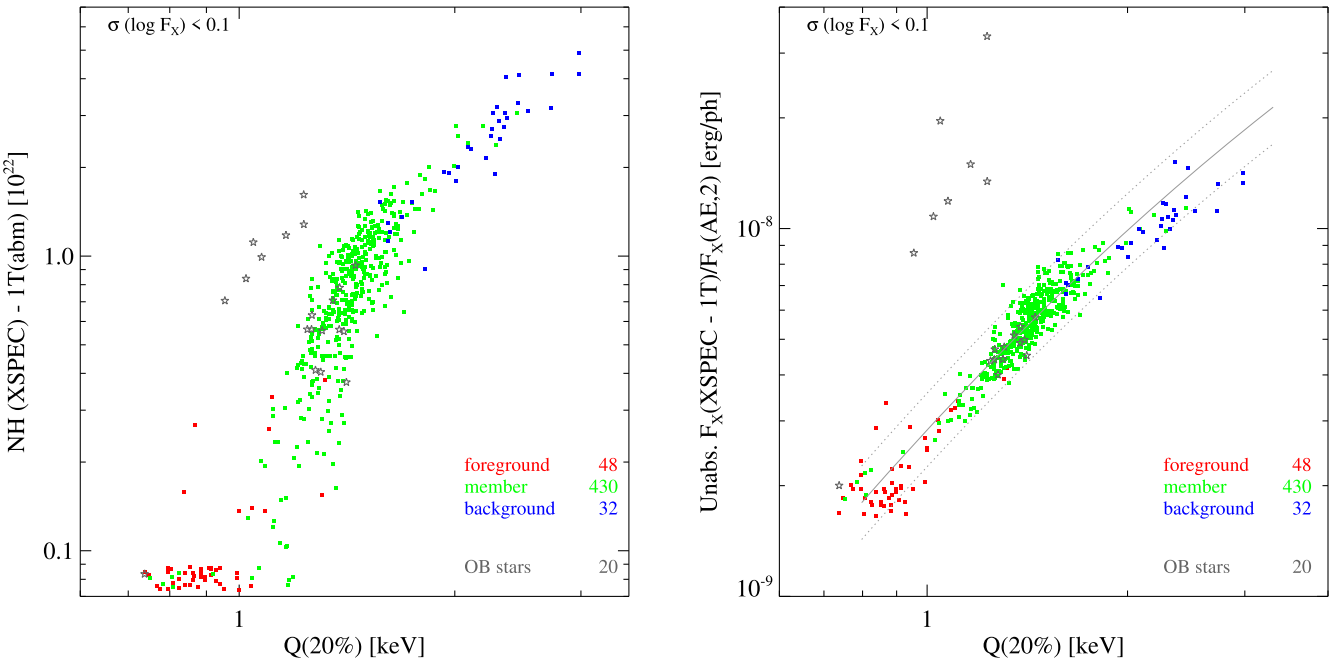

Figure 6. Left: N_H, as estimated through spectral fitting, vs. $Q_{20\%}$, the 20% quantile of the photon energy distribution. Symbols are color coded according to the optical/IR classification, as indicated in the legend. Only stars with mean flux uncertainties <0.1 dex are plotted. Right: ratio of unabsorbed energy flux to observed photon flux plotted as a function of $Q_{20\%}$. Sample and symbols are as in the left panel. The solid line indicates a quadratic fit to the all points except O/B-type stars, and the dashed lines are the same best fit shifted by ±0.1 dex.

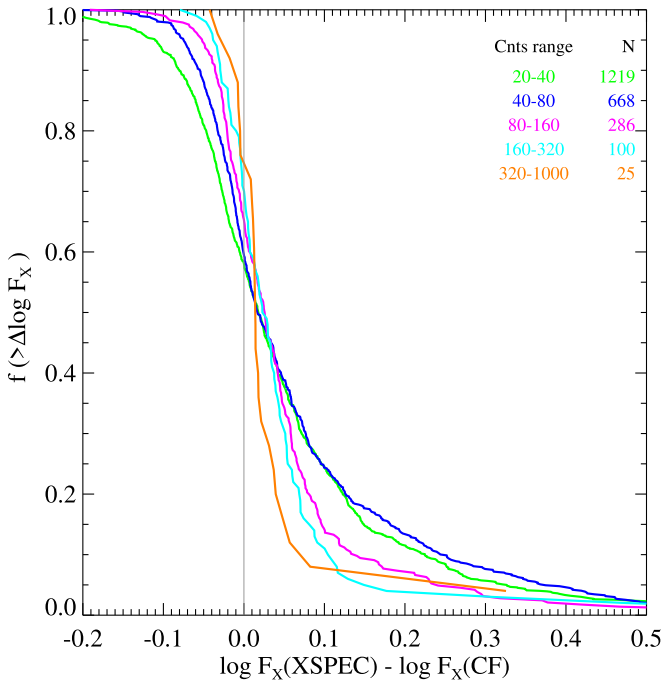

Figure 7. Difference between the logarithmic fluxes obtained from the $Q_{20\%}$-dependent CF and those obtained from spectral fits, for low-mass members in different ranges of net counts.

isothermal spectrum or an absorbed two-temperature thermal spectrum. In this way, we hope to obtain average values of all parameters, including N_H, kT (or kT values), and all the element abundances we can realistically constrain. One possible disadvantage of using stacked spectra is that biases that are hard to control might be introduced by the mixing of spectra with different plasma temperatures and subject to different absorptions. In particular, when using stacked spectra, we should be careful in interpreting the abundances of elements with prominent lines in the 1–2 keV energy range, which is significantly affected by absorption for $N_H \gtrsim 21.0$ cm^{-2}, such as Ne and Mg.

Our second approach is to perform simultaneous fits of the CCD spectra of selected samples of Cyg OB2 X-ray sources. Each source within the sample is allowed to have its own absorption (N_H) and temperature (kT), but, for each element, the model abundance in the parameter estimation scheme is tied as a single parameter across all the difference sources being modeled. These simultaneous fits, performed using the VAPEC model within XSPEC, are computationally intensive, and a simultaneous fit of all X-ray-detected members is not practical. We instead divided the full sample according to ranges of net detected counts and performed simultaneous fits of the spectra in each subsample. Each of these spectral fits is thus independent and can be used to cross-check the results from other subsamples.

In order to validate and tune these two methods and to investigate possible biases, we have first applied the same procedures to the ONC stars using the COUP data.

4.1. Stacked Spectra

We have first considered a representative X-ray spectrum of COUP coronal sources, constructed by stacking the spectra of a sample of sources with reasonable-quality X-ray spectra. Starting from the sample of COUP sources for which estimates of photospheric effective temperatures were available, we selected coronal sources by requiring $T_{\rm eff} < 10^4$ K, thus excluding early-type stars whose X-ray emission is not coronal. We then selected the X-ray sources whose spectral fits by Getman et al. (2005) required two thermal components and had *low* best-fit values of the absorbing column density ($\log N_H < 21.5$ cm^{-2}). The stacked spectrum of the resulting 218 COUP sources contains ∼1.1 million counts. We fit the

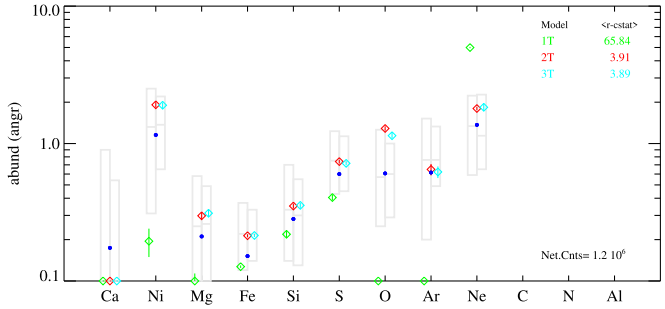

Figure 8. Abundances derived from a stacked spectrum of a sample of COUP sources, namely those with estimates of photospheric effective temperature and mass, with effective temperature less than 10^4 K, and with $\log N_{\rm H}$ (cm^{-2}), from Getman et al. (2005), less than 21.5. Green, red, and cyan points, with 1σ error bars, indicate best-fit abundances obtained from fits with one, two, and three thermal components, respectively. Blue circles indicate the weighted mean of abundances from the simultaneous fits shown in Figure 11. Gray boxes indicate the median and 68% interval of the abundances obtained by Maggio et al. (2007) for stars in their "low-absorption sample" (boxes on the left) and their "count-limited subsample" (boxes on the right).

spectrum with 1T, 2T, and 3T models, in all cases with free abundances for the same elements whose abundances were constrained by Maggio et al. (2007). These were O, Ne, Mg, Si, S, Ar, Ca, Fe, and Ni.

Results are shown in Figure 8: 2T and 3T models yield fits with very similar quality (reduced C-stat $\sim$3.9) and abundances roughly reproducing the Maggio et al. (2007) results, with some potentially interesting differences. Single-temperature fits, instead, are decidedly worse statistically and result in significant biases in the best-fit abundances. The most striking difference with respect to the Maggio et al. (2007) abundances is for oxygen. We will see below that the determination of the oxygen abundance depends heavily on source absorption, and we speculate that the value we derive from a stacked spectrum, the sum of individual spectra subject to different $N_{\rm H}$ values, may be biased.

Next, we have tried to assess, through Monte Carlo simulations, the effects of photon statistics and absorption on the determination of abundances, so as to help in the interpretation of our Cyg OB2 results. Our simulations were based on the 2T model fit to the ONC data discussed above, but with abundances fixed to those of Maggio et al. (2007). Assuming that low-mass stars in the ONC and Cyg OB2 share the same intrinsic X-ray spectrum, we verify our ability to retrieve the input abundances by generating simulated spectra with varying values of $N_{\rm H}$ and different levels of average counting statistics (10^4, 3×10^4, and 10^5 net counts) covering the range of our Cyg OB2 stacked spectra (see below). For each pair of $N_{\rm H}$ and net counts, we produce 1000 simulated spectra and fit each with both 1T and 2T models, initially assuming the solar ANGR abundances from Anders & Grevesse (1989) and fitting the same elements constrained by Maggio et al. (2007). Moreover, we performed additional 1T and 2T fits keeping the oxygen abundance fixed at the Maggio et al. (2007) value ($0.6\times$ solar). Figure 9 shows the mean abundances and relative uncertainties that are expected for two values of $N_{\rm H}$ and three values of net counts.

At low $N_{\rm H}$, input abundances are retrieved when fitting the spectra with 2T models, while 1T models produce biased results, in qualitative agreement with the results on the real ONC stacked spectrum. We are, however, most interested in the results for $N_{\rm H}\sim1.0\times10^{22}$ cm^{-2} (i.e., a representative value for Cyg OB2): (a) The abundance of oxygen cannot be constrained, even with 10^5 counts, and must therefore be fixed (at the Maggio et al. 2007 level); (b) at least $\sim3\times10^4$ counts are needed to constrain Fe and Ne; (c) 1T fits to the absorbed 2T models are statistically *acceptable* (i.e., average reduced C-stat = 1.1, 1.1, and 1.4 at 10^4, 3×10^4, and 10^5 counts, respectively) but produce biased abundances (e.g., low Fe and high Ne).

On the basis of the above results, we present in Figure 10 2T fits to the stacked Cyg OB2 spectra, with O fixed to $0.6\times$ solar (ANGR). The left panel shows abundances derived from stacked spectra constructed for five samples: all members with between 1 and 100 net counts, those with 100–1000 net counts, and those with more than 1, 20, and 100 net counts. Very similar results are obtained, with abundances mainly consistent with those of Maggio et al. (2007), but with some differences in Mg, Si, and Ni (higher Mg and Si and lower Ni). In order to assess the effect of outliers, e.g., misclassified nonmembers or members with peculiar X-ray spectra, we also considered samples with more homogeneous X-ray spectral characteristics, namely those for which the 1T spectral fits yielded 0.5×10^{22} cm^{-2} $< N_{\rm H} < 5.0\times10^{22}$ cm^{-2} and $kT > 1.0$ keV. Results are shown in the right panel of Figure 10. The main difference we see with respect to the full samples is that in the restricted ones the Ni and Si abundances are now consistent with the COUP values.

4.2. Simultaneous Fits

Simulations to assess the effect of simultaneously fitting multiple spectra with 1T models, each with individual $N_{\rm H}$ and kT, and with shared but variable abundances, are not easy to produce. Each simultaneous fit requires a large amount of computing time, especially as the number of sources to fit simultaneously increases. For COUP sources, where sources are fewer and brighter and the $N_{\rm H}$ is lower, we performed simultaneous fits using 2T models, for several independent source samples. Results, shown in Figure 11, largely confirm the abundances of Maggio et al. (2007) and those derived from the fit of the stacked COUP spectra in Figure 8 (although we obtain marginally lower Fe abundances).

The results for Cyg OB2 stars, as shown in Figure 12, are harder to interpret. We are indeed forced to use 1T models (with fixed oxygen). Had we used 2T models, in addition to further increasing the computation time, fit parameters would probably become largely unconstrained. We do not have a firm understanding of how the choice of 1T models for the simultaneous fits biases abundances. Looking at the right panel of the figure (for the somewhat cleaned samples, excluding sources with peculiar spectra), we derive, with respect to Maggio et al. (2007), somewhat higher Fe and Mg (and lower S) abundances. We also notice similarities and some differences with respect to the stacked spectra analysis, the latter possibly due to the aforementioned biases. In particular, focusing on the "cleaned samples," we find the following:

1. Ne appears consistent between the two analyses and with the ONC values (all analyses).
2. The Fe abundances from stacked spectra and simultaneous fits are consistent and only slightly larger than those of ONC stars, as estimated by both Maggio et al. (2007) and our stacked spectra analysis. ONC values from simultaneous fits are instead slightly lower.

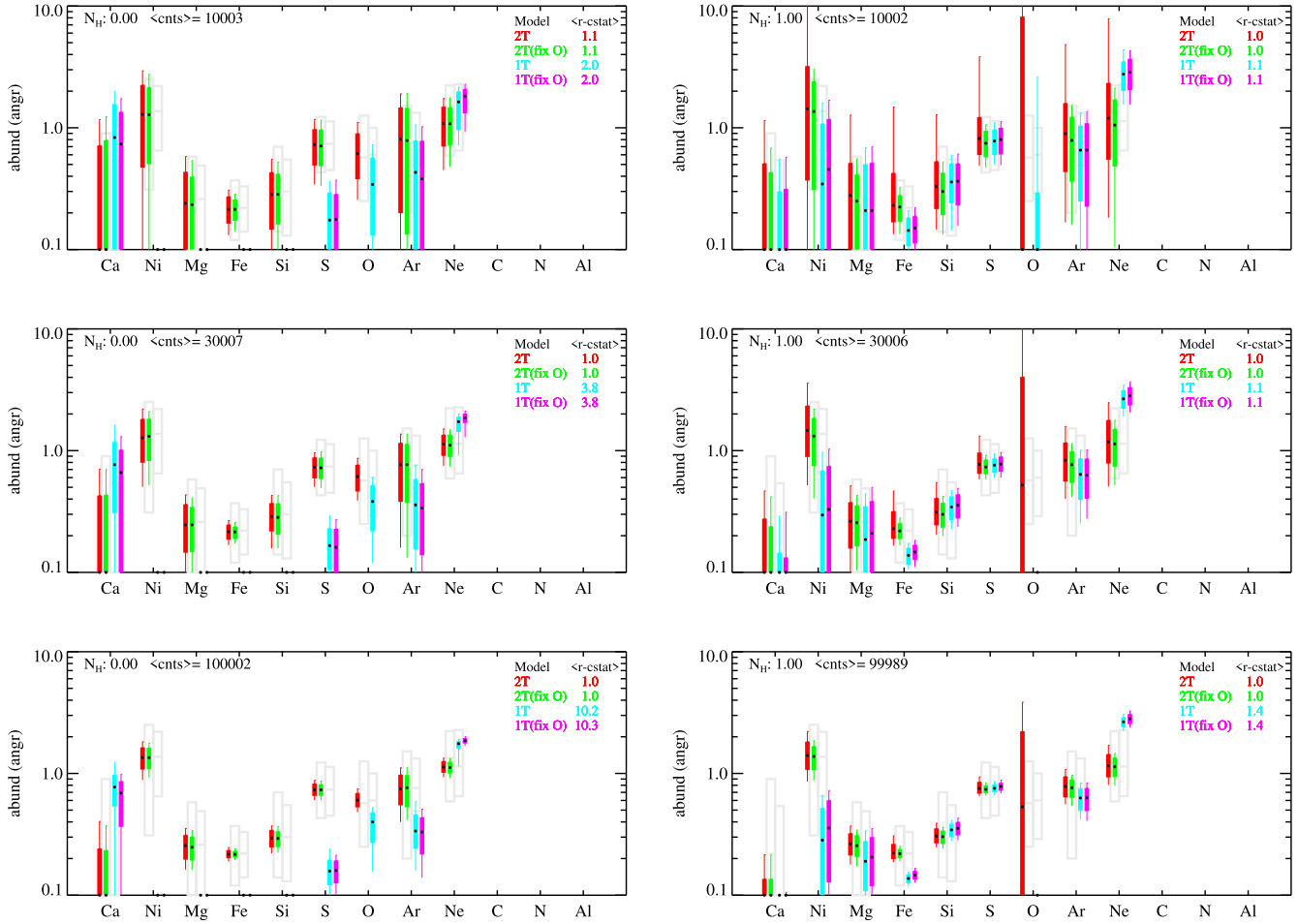

Figure 9. Results of simulations to assess the ability to retrieve element abundances as a function of spectrum absorption ($N_{\rm H}$) and statistics (net counts). See text for details. Each panel refers to a different value of $N_{\rm H}$, 0.0 cm^{-2} in the left column and 1.3×10^{22} cm^{-2} in the right column, and net counts 1×10^4, 3×10^4, and 10×10^4 in the top, middle, and bottom rows, respectively. Within each panel, the thick (thin) vertical bars show the 1σ (90%) dispersions of the abundances derived for each fitted element for a set of 1000 simulations. Median values are indicated by small black circles within the bars. Four estimates are shown, each derived from fitting the simulated spectra with a different model: a 2T model with all shown abundances treated as a free parameter (red bars); a 2T model in which oxygen was fixed at the values derived by Maggio et al. (2007), i.e., 0.6 times the solar ANGR abundances (in green); a 1T model (cyan); and a 1T model with fixed oxygen abundance (magenta). For each spectral model, the average reduced C-stat for fits to the simulated spectra is given in the upper right corner, while the input $N_{\rm H}$ and the average number of net counts in the simulated spectra are given in the upper left corner.

3. The Mg abundances, by the two separate analyses, are consistent and 2–3 times higher than in the ONC (all analyses).
4. The Ni abundances from the two approaches appear to be consistent and similar to the ONC values.

5. Discussion

We now make use of the results of the above analyses to discuss the properties of the coronal plasma in Cyg OB2 stars, in terms of temperature, flux, and abundances, and to investigate the relation between X-ray and optical extinction toward the region.

5.1. Coronal Plasma

At first glance, the coronal plasma properties of Cyg OB2 members differ somewhat from those of other young stars, e.g., those in the ONC, as determined by the COUP studies (Preibisch et al. 2005a). In particular, we successfully fit the X-ray spectra of almost all the Cyg OB2 members with isothermal models, while most of the ONC stars required two thermal components. Moreover, the mean plasma temperature of Cyg OB2 sources, ∼3 keV, appears higher than the average temperature of COUP sources, e.g., ∼2.2 keV for the emission-measure-weighted temperature of low-mass stars with $\log L_X > 30.0$ erg s^{-1} (or ∼2.4 keV for $\log L_X > 30.5$ erg s^{-1}).

As demonstrated in Appendix A, however, it is important to assess the biases introduced by fitting our spectra, which are most likely intrinsically multitemperature, with a single thermal component, even if it is statistically sufficient to represent the observed spectra. This is due mainly to the high extinction, which obscures the low-energy part of the spectra, and, to a lesser extent, to the large distance of Cyg OB2 sources, resulting in spectra with a low S/N. Appendix A describes our efforts to quantify these effects by assuming that our sources have intrinsic spectra similar to those of the closer and much less absorbed young stars in the ONC, as characterized by Getman et al. (2005), and in particular to those whose spectrum was fit with two thermal components. Using these templates, we simulate the effect of higher extinction and larger distance on the spectral characterization of the sources.

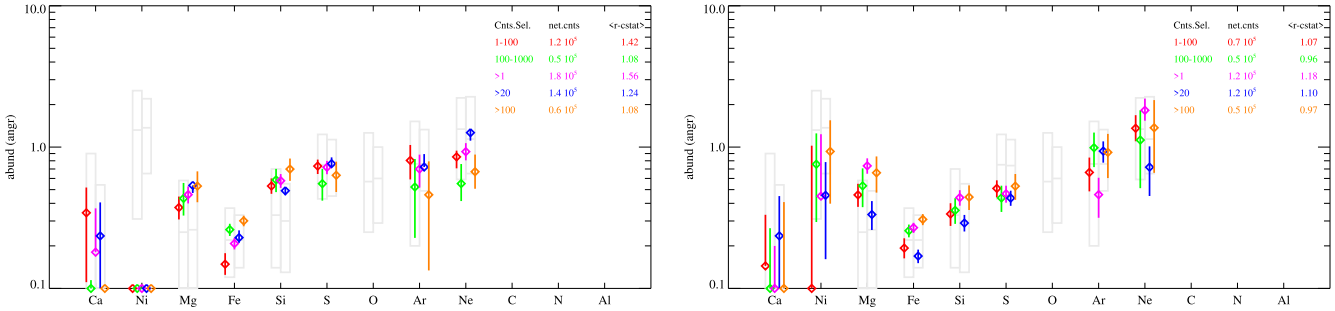

Figure 10. Abundances derived from a stacked spectrum for five samples of Cyg OB2 members selected in five different ranges of net counts, as indicated in the legend in the upper right corner of each panel. The left panel refers to the full samples of members, and the right panel refers to samples of members for which the 1T spectral fits yielded *reasonable* parameters (0.5×10^{22} cm^{-2} $< N_{\rm H} < 5.0 \times 10^{22}$ cm^{-2} and $kT > 1.0$ keV). In all cases, stacked spectra were fit with a 2T model with the oxygen abundance fixed to the Maggio et al. (2007) values (0.6 × solar, in the ANGR table). Note that in a small number of cases upper or lower error uncertainties are not plotted, as their estimation within XSPEC failed.

We conclude that if our Cyg OB2 sources have X-ray spectra that are intrinsically similar to those of their ONC counterparts, (i) our isothermal model fits are consistent with intrinsically two-temperature spectra; (ii) our best-fit values of $N_{\rm H}$ are underestimated, on average, by $\sim 2 \times 10^{21}$ cm^{-2} or, considering the average $N_{\rm H}$ of Cyg OB2 stars, ∼20%; (iii) our source fluxes are also underestimated by ∼0.11 dex; and (iv) the plasma temperatures we obtain are similar (0.1 keV lower, on average) to those of the hot component of a two-temperature model (and ∼0.40 keV higher than the average temperature). Overall, the Cyg OB2 X-ray spectra thus appear compatible with those of ONC stars.

Figure 13 shows the run of $L_{\rm X}$ with detected net photons, the relation between $N_{\rm H}$ and kT, and the relation between $L_{\rm X}$ and the latter two parameters. Only sources with relatively well-determined parameters are plotted, i.e., with 1σ uncertainties on the plotted quantities <0.2 dex. Focusing on low-mass Cyg OB2 members, i.e., excluding foreground and background objects, as well as OB members, we notice several points. First, $N_{\rm H}$ and kT are anticorrelated. This is most likely a spurious effect owing to the well-known anticorrelated shape of the χ^2/C-stat space in the two fit parameters. It is also fully confirmed by our simulations of ONC sources performed at fixed input $N_{\rm H}$ showing the exact same trend. $L_{\rm X}$ and $N_{\rm H}$ appear mostly uncorrelated, although a dearth of high-$L_{\rm X}$, low-$N_{\rm H}$ stars may be observed. Again, our simulations of ONC sources with fixed input $N_{\rm H}$ reproduce this trend, which can thus be considered a spurious effect owing to the statistical uncertainties on $N_{\rm H}$ and the expected correlation between these uncertainties and the uncertainties on the absorption correction for the flux, and thus on $L_{\rm X}$. Finally, $L_{\rm X}$ and kT appear directly correlated. Our simulations of ONC sources instead produce an inverse correlation, which is easily understood in terms of the spurious $N_{\rm H}$–kT and $L_{\rm X}$–$N_{\rm H}$ (anti)correlations discussed above. The observed direct correlation can thus be considered even more significant and physical. This is in qualitative agreement with previous results on the correlation between coronal X-ray flux and plasma temperature (e.g., Peres et al. 2004; Preibisch et al. 2005a; Johnstone & Güdel 2015).

5.2. Coronal Abundances

The abundances of elements in stellar coronae are known to differ from those in the underlying photosphere (e.g., Drake et al. 1996; Drake 2002; Laming 2015). While the exact mechanism or mechanisms responsible for the chemical fractionation have not been securely identified, the differences appear to depend on both magnetic activity level and spectral type (Drake 2003; Telleschi et al. 2007b; Laming 2015; Wood et al. 2018). Our Cyg OB2 sample of young low-mass stars represents a potentially valuable set of observations with which to investigate chemical fractionation further.

Overall, our abundance results for the T Tauri stars in Cyg OB2, presented in Section 4, appear to show characteristics of the "inverse first ionization potential (FIP) effect" (iFIP), in which elements with low FIP (FIP $\leqslant$ 10 eV, e.g., Si, Mg, Fe) are depleted relative to elements with high first ionization potentials (FIP $\geqslant$ 10 eV, e.g., N, Ne, Ar). This abundance pattern is opposite to that characterizing the solar corona, in which low-FIP elements are enhanced (e.g., Laming et al. 1995). While hints of iFIP abundance patterns were present in early CCD-resolution spectra of active stars obtained by the Advanced Satellite for Cosmology and Astrophysics (ASCA; see, e.g., Drake et al. 1996 for a review), high-resolution spectra obtained by Chandra and XMM-Newton provided the first definitive and detailed iFIP abundance information (Brinkman et al. 2001; Drake et al. 2001). Empirically, for both PMS stars and main-sequence stars with little or moderate magnetic activity, the presence and strength of a solar-like FIP effect or an iFIP effect depend primarily on the spectral type (Güdel et al. 2007; Telleschi et al. 2007a; Laming 2015; Wood et al. 2018). The most active stars, however, seem to depart from this relationship and to show strong iFIP abundance patterns (Wood et al. 2018). While the mechanism underlying the chemical fractionation responsible for FIP-based effects has not been firmly identified, the most promising explanation is based on the ponderomotive forces experienced by ions in the chromosphere (e.g., Laming 2009).

The abundance analysis of Chandra observations of young stars in the ONC by Maggio et al. (2007), and now also in Cyg OB2, firmly establishes T Tauri stars in the iFIP category, in keeping with expectations based on their "saturated" levels of magnetic activity. The dependence of FIP bias on spectral type (Wood et al. 2018) cannot easily be investigated with our data set. However, we note that the Fe abundances and Fe/Ne ratios from our stacked spectra analysis (Figure 10) for stars with more or less than 100 detected counts (and thus, on average, different $L_{\rm X}$; see Figure 13) are both consistent with the trends of higher Fe and lower Fe/Ne for earlier-type (and X-ray-brighter) stars (Güdel et al. 2007; Telleschi et al. 2007a; Wood et al. 2018).

5.3. X-Ray versus Optical Extinction

We used our extensive data set to investigate the relation between optical extinction, A_V, and X-ray absorption, as

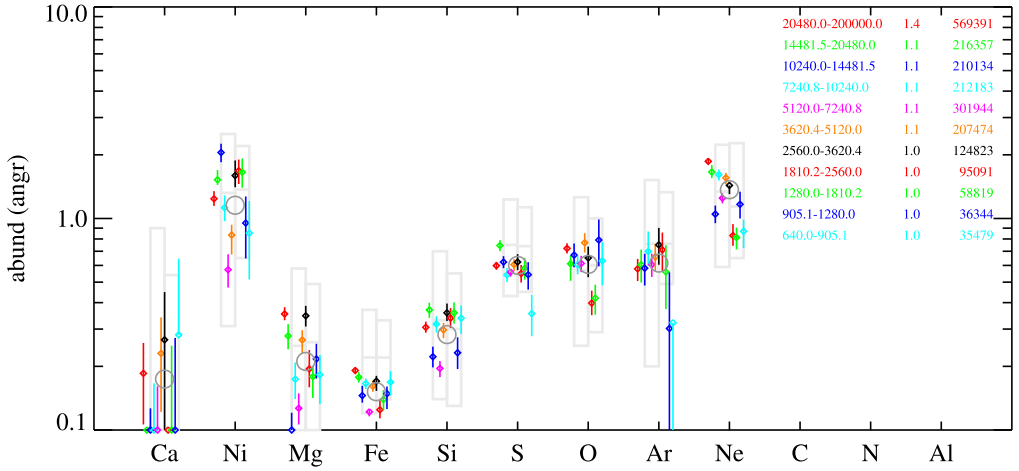

Figure 11. Abundances derived from simultaneous fits of different and independent samples of ONC sources from the COUP survey. The samples are selected so as to contain sources with net counts in selected ranges, plotted with decreasing counts from left to right, as indicated in the legend (note that some colors are repeated). The spectra were fit with 2T models, allowing $N_{\rm H}$ and the two temperatures to vary for each source. Reduced C-stat values of the fits and total number of counts in the spectra are indicated beside each count range. Large open circles indicate the uncertainty-weighted mean of the abundances for all count ranges.

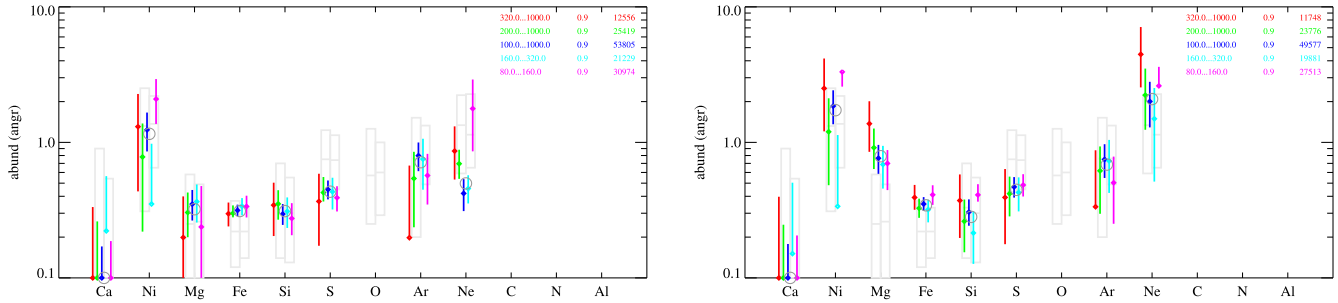

Figure 12. Abundances derived from simultaneous fits for different (and not all independent) samples of Cyg OB2 members. In the left panel, samples are selected so as to contain all members detected in X-rays with net counts in selected ranges, as indicated in the legend in the upper right corner. Spectra were fit with 1T models, allowing $N_{\rm H}$ and kT to vary for each source. Reduced C-stat values for the fits and the total number of counts in the spectra are indicated beside each count range. Gray circles indicate uncertainty-weighted mean abundances computed from all values with fully defined uncertainties. The right panel is analogous to that on the left, but samples are restricted to X-ray sources whose individual 1T spectral fits yield $N_{\rm H}$ and kT values that are consistent with the member population (more specifically, 0.5×10^{22} cm$^{-2} < N_{\rm H} < 5.0 \times 10^{22}$ cm^{-2} and $kT > 1.0$ keV).

parameterized by the hydrogen column density $N_{\rm H}$. The $N_{\rm H}/A_V$ ratio is a measure of the gas-to-dust ratio of the interstellar medium (ISM), in our case toward and in the environment of our Cyg OB2 stars. While A_V depends on the content and properties of dust in the ISM, the X-ray absorption depends on the column density of heavy elements, which, for a given chemical composition of the ISM, is proportional to $N_{\rm H}$. Different techniques and spectral bands (UV, radio, and X-rays) have been used to estimate the $N_{\rm H}$ column density and the optical extinction toward a variety of objects—stars of different kinds and in different environments, supernova remnants, X-ray binaries (see, e.g., Zhu et al. 2017, for a summary). The precise value of the $N_{\rm H}/A_V$ ratio, as well as its eventual dependence on spatial and/or physical parameters, is debated. Several slightly different ratios have been determined even when using the same objects and spectral bands, e.g., 1.8×10^{21} cm^{-2} mag^{-1} and 2.2×10^{21} cm^{-2} mag^{-1} by Predehl & Schmitt (1995) and Ryter (1996), respectively.

A few determinations have specifically targeted star-forming regions, often finding somewhat lower $N_{\rm H}/A_V$ ratios with respect to the "galactic values" referenced above. Vuong et al. (2003), for the highly absorbed X-ray spectra of stars in the ρ Ophiuchi region, found $N_{\rm H}/A_V = 1.6 \times 10^{21}$ cm^{-2} mag^{-1} when adopting "standard" ISM abundances and transforming the J-band extinction to A_V using a standard extinction law with $R_V = 3.1$. This $N_{\rm H}/A_V$ ratio is somewhat lower than most estimates and has since been adopted in several works (e.g., Getman et al. 2011; Skinner & Güdel 2017).

The above derivation was obtained from a sample of relatively absorbed stars, most with $N_{\rm H} \gtrsim 10^{22}$ cm^{-2} (median $\sim 2 \times 10^{22}$ cm^{-2}). Indeed, because of the large relative uncertainties in the determination of $N_{\rm H}$ from X-ray spectral fits, especially for small $N_{\rm H}$ values, the relation is more easily investigated using stars in more absorbed regions, just like ρ Ophiuchi and Cyg OB2. More recently, Hasenberger et al. (2016) have investigated the matter using $N_{\rm H}$ values obtained by the COUP collaboration based on fitting X-ray spectra of stars in the ONC (Getman et al. 2005) and optical extinction values obtained from spectral types, near-IR colors, and a standard extinction law. An $N_{\rm H}/A_V$ ratio of 1.4×10^{21} cm^{-2} mag^{-1} was obtained, which is even lower than that of Vuong et al. (2003).

Our survey of absorbed and reddened stars in Cyg OB2 presents a large sample with which to further investigate the gas-to-dust ratio in or toward star-forming regions. We have used the $N_{\rm H}$ values from our spectral fits and the A_V values derived from the optical photometry (Guarcello et al. 2023b) for a new estimate. Both are representative of the total extinction toward the star, including contributions from the

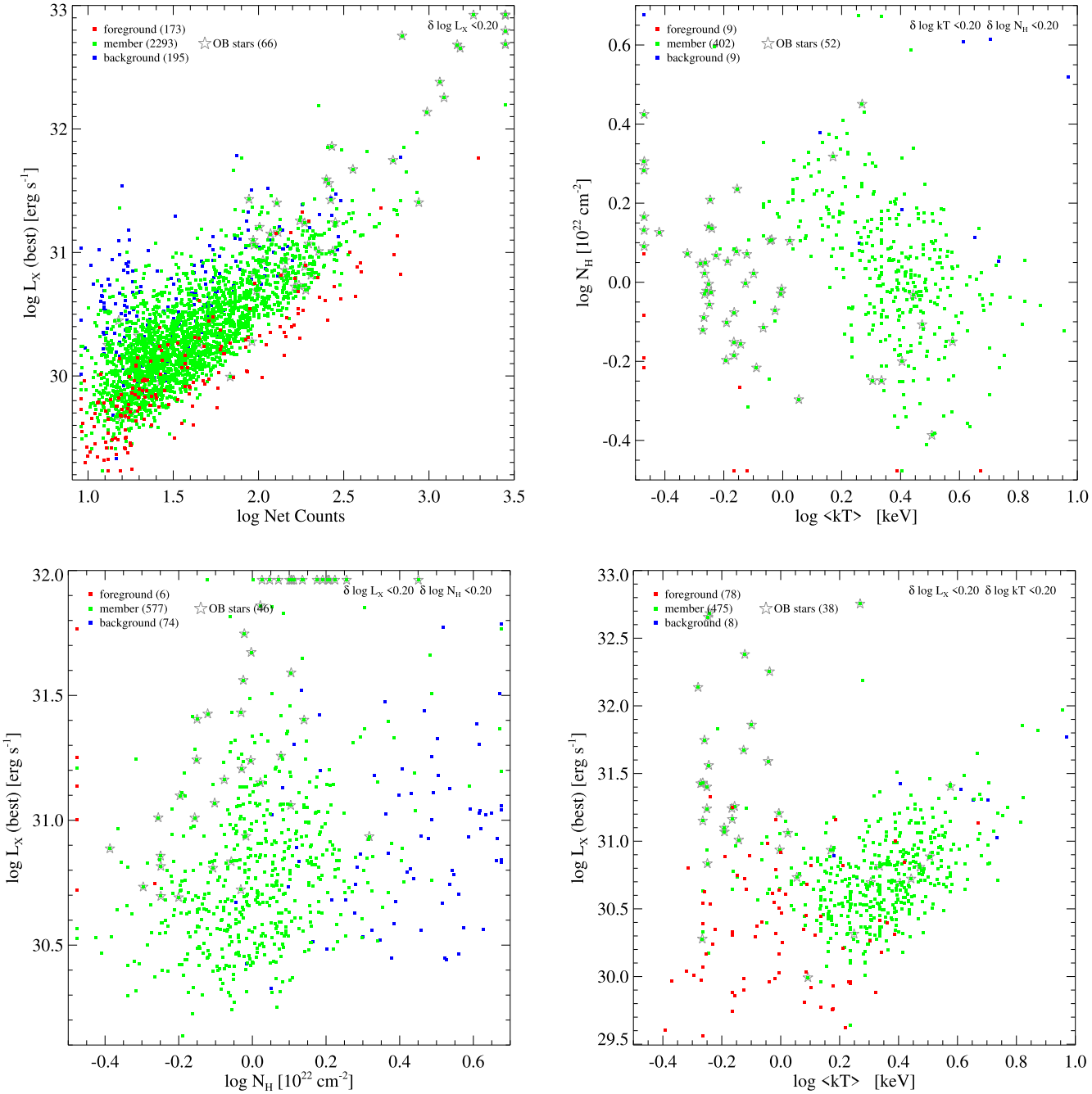

Figure 13. Top left: X-ray luminosities vs. net detected counts, separately for members, foreground objects, and background objects, as indicated in the legend in the upper left corner. OB stars are marked with a star. The sample is limited to sources with 1σ uncertainty on the X-ray luminosities <0.2 dex (as indicated in the upper right corner). A handful of stars in the upper right corner, with L_X and/or net counts larger than the plot limits, are plotted close to the axes. Top right: same as the top left panel, but for N_H vs. average kT. Bottom left: same as the top left panel, but for L_X vs. N_H. Bottom right: same as the top left panel, but for L_X vs. average kT.

ISM toward the Cyg OB2 complex, the molecular cloud, and the circumstellar environment (e.g., disks and envelopes). The circumstellar contribution is, however, unlikely to dominate for Cyg OB2 members, since stars with and without evidence for circumstellar disks share similarly large extinctions. The molecular cloud is, moreover, also unlikely to dominate the total extinction, since previous studies point toward a large contribution from the Great Cygnus Rift, in the foreground (Sale et al. 2009; Gottschalk et al. 2012). We discuss results obtained adopting A_V values derived by Guarcello et al. (2023b) using both the Fukugita et al. (1996) and Fitzpatrick & Massa (2007) optical extinction laws. Adopting the Fitzpatrick & Massa (2007) extinction law, the left panel of Figure 14 shows the N_H versus A_V scatter plot for a sample of 239 Cyg OB2 members with more than 100 detected net X-ray photons and for which the 1σ uncertainty on N_H was less than 0.30×10^{22} cm^{-2}. Statistical tests indicate that the two quantities are correlated with high confidence. We estimate our best-fit N_H/A_V ratio by both taking the median ratio of all points and performing an ordinary least-squares linear fit (with fixed intercept). The results in Figure 14 are $N_H/A_V = 2.0$ and 1.8×10^{21} cm^{-2} mag^{-1}, respectively, for the median ratio and the linear fit, which are compatible with galactic values. Adopting the larger A_V values resulting from the extinction

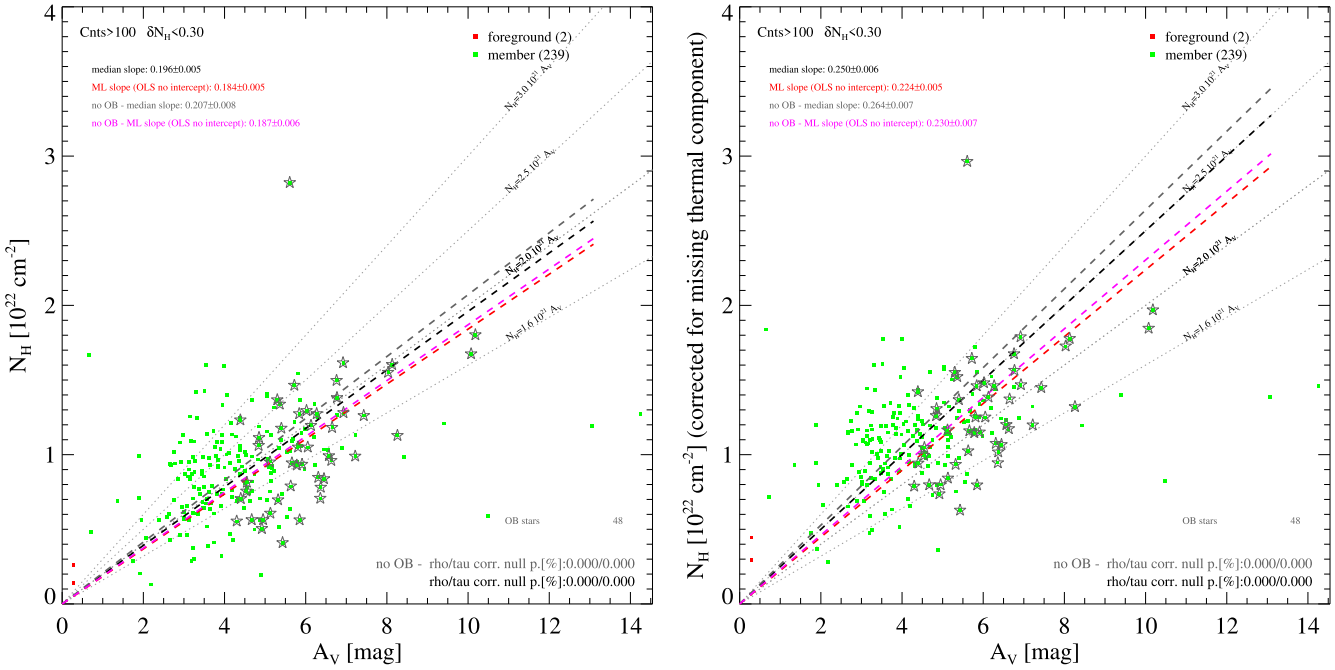

Figure 14. Left: $N_{\rm H}$ vs. A_V for Cyg OB2 members with more than 100 X-ray counts and 1σ uncertainties on $N_{\rm H}$ less than 0.3×10^{21} cm^{-2} mag^{-1}. OB stars are marked by star symbols. Results of Spearman's (ρ) and Kendall's (τ) rank correlation tests are indicated in the lower right corner both for the full sample of stars and excluding the OB stars. Two estimates for the slope of the correlation are given in the upper left corner, again both for the full sample and excluding the OB stars. These are also illustrated by thick dashed lines. Right: same as the left panel, but using "bias"-corrected $N_{\rm H}$ values.

law of Fukugita et al. (1996), however, the two estimates become, respectively, 1.6×10^{21} cm^{-2} mag^{-1} and 1.5×10^{21} cm^{-2} mag^{-1}, consistent with Vuong et al. (2003). Note that Figure 14 also shows the results of the same analysis restricted to low-mass stars, i.e., excluding the 48 OB stars marked by star symbols. The latter stars might in principle behave differently, e.g., because of a different location in the cloud, their clearing of ambient material, and/or the different approach used to estimate A_V. The differences in the $N_{\rm H}/A_V$ slopes with respect to the full sample, however, are not significant.

As already discussed (Section 5.1) and demonstrated in Appendix A, however, the isothermal models used to fit the Cyg OB2 X-ray spectra, which are statistically adequate owing to their high extinction and poor statistics, introduce significant biases. Using the ONC stars as templates, we simulate the effect of higher extinction and larger distance on the spectral characterization of the sources. We conclude that our $N_{\rm H}$ values are systematically underestimated by an amount that depends on $N_{\rm H}$, and which is $\sim 2.0 \times 10^{21}$ cm^{-2}, or 20%, at the typical extinction of Cyg OB2. We can correct our $N_{\rm H}$ values for this bias by adding the $N_{\rm H}$-dependent offsets shown by the black filled symbols in Figure 15 (bottom right panel). The right panel of Figure 14 shows the result of this correction for the case of the A_V values derived from the Fitzpatrick & Massa (2007) extinction law. The $N_{\rm H}/A_V$ ratios in this case become 2.5–2.2 cm^{-2} mag^{-1}. Even when adopting the Fukugita et al. (1996) optical extinction law, the $N_{\rm H}/A_V$ ratio increases to 2.0–1.9 cm^{-2} mag^{-1}, becoming compatible with the Galactic values.

We conclude that the stars in Cyg OB2 do not support the low value of $N_{\rm H}/A_V$ found in ρ Ophiuchi by Vuong et al. (2003) and in the ONC by Hasenberger et al. (2016). If those results are correct, then it may point to a variation of the gas-to-dust ratio in different star-forming regions and the ONC and ρ Ophiuchi being more dust-rich than Cyg OB2. This is perhaps not unreasonable given the very different and milder radiation environments of those regions compared with the intense UV–X-ray and particle radiation fields of Cyg OB2 that might be expected to cause more dust destruction (e.g., Jones 2004). If, however, the extinction toward Cyg OB2 is dominated by the Great Cygnus Rift, the $N_{\rm H}/A_V$ ratio toward the Cyg OB2 stars would provide a confirmation of the spatial invariance of the galactic gas-to-dust ratio (e.g., Zhu et al. 2017).

6. Summary

We have derived fluxes and X-ray spectral parameters for the X-ray sources detected in our Chandra Cygnus OB2 survey, paying particular attention to the young members of the region. Most X-ray sources were detected with few photons and have poorly defined X-ray spectra. Care was taken to minimize statistical and systematic uncertainties. For stars with >20 counts we fitted isothermal models with three free spectral parameters: kT, $N_{\rm H}$, and unabsorbed flux. However, in order to limit statistical uncertainties for the fainter Cyg OB2 members, we often restricted the range of allowed $N_{\rm H}$ and kT values to the ranges defined by the brighter members. The chemical abundances of the emitting plasma were fixed at the values estimated by Maggio et al. (2007) for similarly young stars in the ONC star-forming region.

A different approach was adopted for X-ray sources detected with <20 net counts: 20% quantiles of the detected photon energy distributions were demonstrated to be effective indicators of $N_{\rm H}$ and of the CF between detected photon flux and unabsorbed energy flux. Quantile versus CF relations were defined from the X-ray-bright low-mass members with well-defined spectral models and then applied to the fainter sources. This effectively assumes that these fainter sources have X-ray

spectra and, in particular, absorbing hydrogen columns, upon which the CFs depend most critically, that are similar to those of the brighter sources.

These results of our X-ray spectral fitting will be more thoroughly used in a forthcoming investigation of the general state of magnetic activity in Cyg OB2 members. Here, we have additionally investigated the gas-to-dust ratio toward the Cyg OB2 stars by estimating the ratio of X-ray to optical extinction, i.e., the $N_{\rm H}/A_V$ ratio. We find that, once systematic biases are taken into account, the $N_{\rm H}/A_V$ ratio toward our Cyg OB2 stars is compatible with typical Galactic values and significantly larger than the value estimated toward other lower-mass star-forming regions, such as ρ Ophiuchi (Vuong et al. 2003) and the ONC (Hasenberger et al. 2016).

Finally, we have attempted to verify our assumptions on the plasma abundances through ensemble analyses of the spectra of Cyg OB2 members. We conclude that, overall, the abundances of the Cyg OB2 stars are compatible with those derived for the slightly younger but similarly active ONC members. In both cases the abundance patterns indicate that an inverse FIP effect is at work, consistent with previous results for very active main-sequence stars.

Acknowledgments

M.G.G. and N.J.W. were supported by Chandra grant GO0-11040X during the course of this work. M.G.G. and E.F. acknowledge financial contributions from the grant PRIN-INAF 2012 (P.I. E. Flaccomio) and from the ASI-INAF agreement No. 2017-14-H.O. N.J.W. acknowledges a Royal Astronomical Society Research Fellowship. M.M., J.J.D., and V.K. were supported by NASA contract NAS8-03060 to the Chandra X-ray Center and thank the directors B. Wilkes, P. Slane, and the CXC science team for continuing support and advice. J.F.A.-C. is a researcher of CONICET and acknowledges their support.

Software: XSPEC (v12.9; Arnaud 1996), ACIS Extract (Broos et al. 2010).

Appendix A
The ONC at the Distance and Extinction of Cygnus OB2

The comparison of X-ray luminosities and spectral parameters of our Cyg OB2 stars with those of young stars in other star-forming regions is complicated by their different distances and extinctions, as well as by the different observing strategies adopted. The effect of the relatively large extinction suffered by the Cyg OB2 sources ($\sim 1 \times 10^{22}$ cm^{-2}) is particularly relevant, as it deprives source spectra of their low-energy photons, possibly affecting the reconstruction of intrinsic spectra and the derivation of plasma temperatures, extinction, and intrinsic X-ray fluxes.

In order to facilitate the above comparison, we here describe Monte Carlo simulations principally meant to illustrate what the Chandra observations described in this paper would have seen had the Cyg OB2 population been replaced by the young stars in the well-studied ONC star-forming region. We will assume that the intrinsic X-ray spectra of the ONC population are well described by the emission models obtained from the observations of COUP (Getman et al. 2005). Given the exposure time of the COUP observations ($\sim$850 ks), the relatively low extinction of the ONC stars, and their closer distance, this sample is arguably the best characterized among all star-forming regions.

We adopt the following strategy: First, we assign each of the $\sim$1500 COUP sources with an emission model to the position of a random source in our Cyg OB2 Chandra catalog and adopt the response function, effective area, exposure time, and background spectrum of the Cyg OB2 source. We then produce simulated source spectra by adopting the COUP one- or two-temperature emission models from Getman et al. (2005)[16] but changing $N_{\rm H}$ to a new value, e.g., to the median Cyg OB2 value (1.0×10^{22} cm^{-2}), and reducing the normalization(s) of the emission component(s) by the distance dilution factor. Finally, we fit the spectra with absorbed isothermal models, using the exact same strategy, models, and abundances we adopted for our Cyg OB2 sources. This process is repeated 10 times for each COUP source, each time adopting the characteristics (position, exposure time, response, background) of a new random Cyg OB2 source. We thus simulate $\sim$15,000 X-ray sources, the great majority with the X-ray characteristics of $\sim$1 Myr old stars and spanning the whole mass range from $\sim$0.1 to $\sim$38 $M_\odot$. Source spectra were simulated using either one or two thermal components, following the original description of their COUP spectra. In the following, we will mostly focus on the subset of these spectra with two thermal components, under the reasonable hypothesis that these are the most representative of underlying "multitemperature" spectra. The 1T COUP spectra will, however, serve as a useful cross-check, as well as a means to isolate the effect on the best-fit parameters of varying the absorption and emission models. The simulations were repeated for 12 different $N_{\rm H}^{\rm out}$ values of the simulated populations, from zero to 4×10^{22} cm^{-2}. For comparison with our Cyg OB2 results, we will focus on the cases with $N_{\rm H}^{\rm out} \sim 1.0 \times 10^{22}$ cm^{-2} and consider only the simulated sources with (background-subtracted) simulated spectra containing more than 100 counts. The resulting samples vary in size depending on the simulation set, as shown in the top left panel of Figure 15: for $N_{\rm H}^{\rm out} \sim 1.0 \times 10^{22}$ cm^{-2} the sample with 2T input models and >100 simulated counts comprises $\sim$600 simulated sources, which may be compared to the $\sim$400 Cyg OB2 sources observed with >100 counts.

For our first experiment we adopt the same emission and absorption models (vapec and tbabs) and the same coronal abundances (Maggio et al. 2007) for both the simulated spectra and the fit models. In this way we mean to test the effects of the increased distance and absorption on the choice of best-fit model (i.e., 1T vs. 2T) and resulting parameters. The main results of these simulations are shown by black symbols in Figure 15. First, we note that, as shown in the top right panel of the figure, isothermal fit models generally provide statistically adequate fits to the diluted and absorbed 2T spectra, at least for $N_{\rm H}^{\rm out} \gtrsim 0.7 \times 10^{22}$ cm^{-2}. In addition, as shown in the two bottom panels, we quantify the resulting biases in best-fit $N_{\rm H}$ values and unabsorbed X-ray fluxes, both of which turn out to be significantly underestimated when fitting 2T spectra with isothermal models.

For $N_{\rm H}^{\rm out} = 1.0 \times 10^{22}$ cm^{-2}, i.e., about the median value we obtain for our Cyg OB2 sources, we see that $N_{\rm H}$ values are actually systematically underestimated by $\sim 0.21 \times 10^{22}$ cm^{-2}

[16] The absorption and emission models used in XSPEC were MEKAL and WABS, respectively, and abundances were set to 0.3 solar, according to the ANGR tabulation.

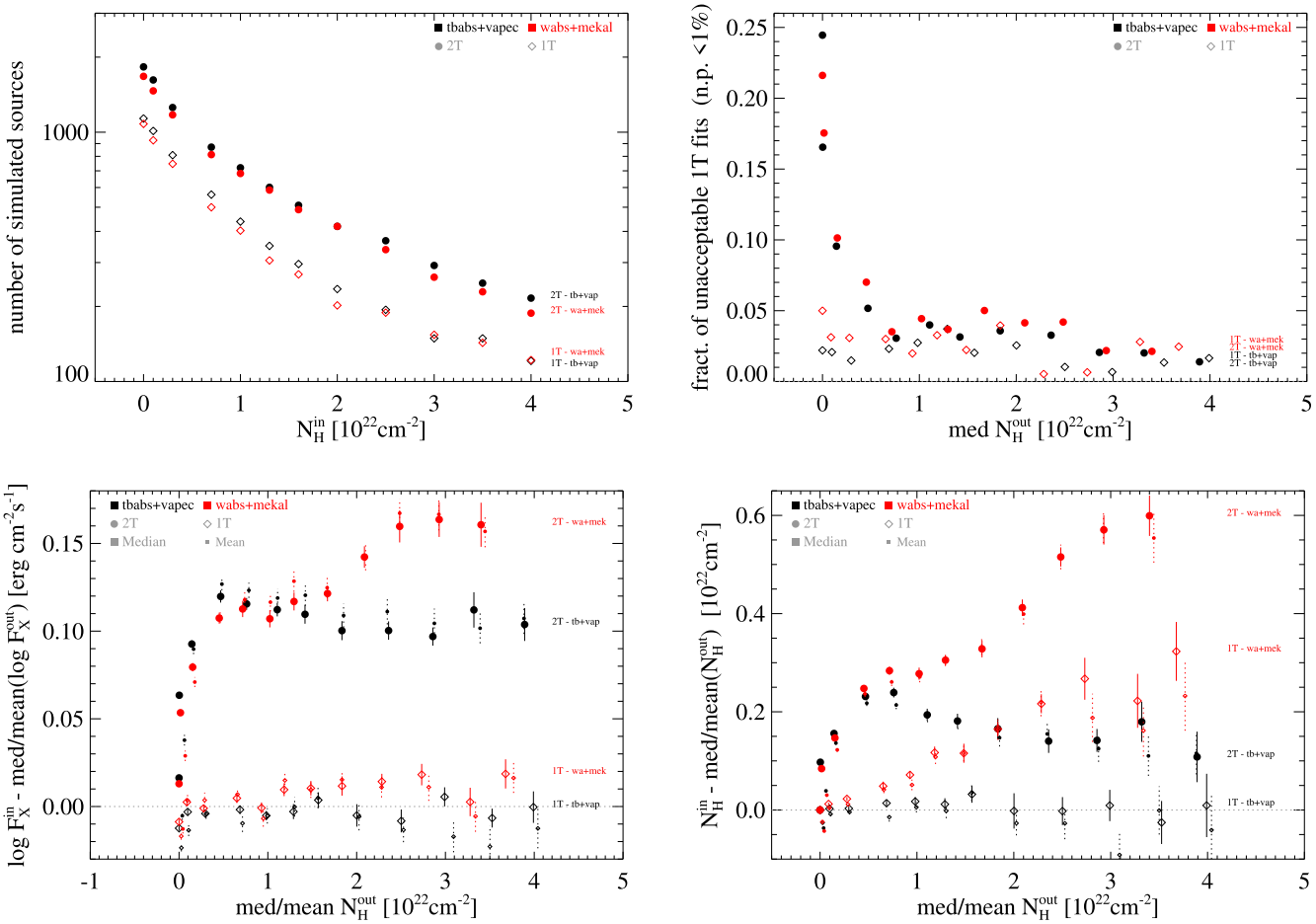

Figure 15. Results of simulations to assess the effect of varying X-ray absorption, N_H, on our ability to discriminate between 1T and 2T models and to retrieve X-ray fluxes and N_H values when fitting X-ray spectra with absorbed isothermal models. The top left panel shows the number of simulated sources with more than 100 net counts for each simulation set, i.e., for each value of N_H^{in}. Each plotted set is labeled close to its rightmost point, and a legend is also provided in the upper right corner. Figures for two-temperature and isothermal input models are plotted separately, as filled circles and open diamonds, respectively. Black symbols refer to simulations in which the 1T fitted model is consistent with the input spectrum (1T or 2T), i.e., the absorption and emission models are, respectively, TBABS and VAPEC with Maggio et al. (2007) abundances. The red symbols instead refer to the case in which the input spectra are described by the older WABS and MEKAL models (with ANGR abundances), while the fitted model is as above. Next, in the top right panel, we show the fraction of "unacceptable" spectral fits as a function of median N_H^{out}, again separately for 1T and 2T simulated input spectra and for the two different fit models. Unacceptable fits are defined as those with null probability, as given by the XSPEC GOODNESS command, of less than 1%. Note that the fraction of unacceptable spectral fits, i.e., those for which a second thermal component might improve the fit, is always low for isothermal input models (as expected), as well as for 2T input models for which the N_H^{out} is $\gtrsim 0.7 \times 10^{22}$ cm^{-2}. The bottom left panel shows the median (and mean) difference between the reconstructed unabsorbed flux and the flux of the input model as a function of the median (and mean) best-fit N_H. Large and small symbols, both with error bars, indicate whether median or mean values are considered for each simulation set. The bottom right panel analogously shows, as a function of median/mean best-fit N_H, the difference between models and mean/median best-fit N_H.

and unabsorbed fluxes by 0.11–0.12 dex, depending on whether we consider mean or median values.

Finally, for a more direct comparison with the COUP results, we then repeated the Monte Carlo simulations adopting the same exact input models provided by Getman et al. (2005) for the ONC sources, i.e., adopting the WABS and MEKAL absorption and emission models, respectively, and 30% solar abundances according to the Anders & Grevesse (1989) tabulation. These models are most representative of the actual observed COUP spectra. The results, shown by red symbols in Figure 15, were somewhat similar to the previous set of simulations, at least for $N_H^{out} \sim 1.0 \times 10^{22}$ cm^{-2}. We can isolate the effect of changing the absorption and emission model prescriptions by looking at isothermal spectra. We see that the N_H values originally reported by Getman et al. (2005) based on the WABS × MEKAL models with 0.3 times the solar abundances according to Anders & Grevesse (1989) are systematically lower, by 7%–8%, with respect to those obtained with TBABS × VAPEC and Maggio et al. (2007) abundances.

When looking at best-fit temperatures (not shown), the single-temperature fits of two-component spectra yield temperatures that are 0.1–0.2 keV cooler than the hot component of the input spectrum. At $N_H^{out} \sim 1.0 \times 10^{22}$ cm^{-2}, i.e., for the stars of Cyg OB2, the median kT is 0.1 keV cooler than the hot component and ∼0.4 keV hotter than kT_{av}, the average, emission-measure-weighted temperature of the input spectra. Since the median kT_{av} of ONC sources with $\log L_X > 30.5$ erg s^{-1} (approximately the lower end for Cyg OB2 sources with >100 counts) is ∼2.4 keV and the median kT for our Cyg OB2 low-mass members with >100 counts is ∼3.3 keV, our results seem to indicate that the X-ray-emitting plasma of low-mass stars in the Cyg OB2 region might be slightly hotter than in ONC stars. However, because of the L_X–kT correlation (see Section 5.1), and since we are comparing flux-limited samples, the difference might be explained by a difference in the composition of the two samples (e.g., due to

uncertainties in the distance to Cyg OB2). Moreover, a greater incidence of hot flaring emission in the shorter Cyg OB2 observations might also explain the small difference in median plasma temperatures. Finally, we stress that the biases we have quantified here should be taken into account when comparing X-ray fluxes and $N_{\rm H}$ values between regions subject to low and high absorption, such as, respectively, the ONC and Cyg OB2.

Appendix B
Biases from Abundance Assumptions

We assess here the effects of different choices of abundance sets for the results of our spectral fitting process. We repeat our spectral analysis (1T fits) using, in addition to our default abundance set (Maggio et al. 2007), those published for SU Aur and V410 Tau in Table 5 of Telleschi et al. (2007b). Figure 16 summarizes the comparison among the three abundance sets. The top and bottom rows refer to a different pair of abundance sets, Maggio et al. versus SU Aur and Maggio et al. versus V410 Tau, respectively. Each column refers to a different fit parameter, from left to right: unabsorbed flux, $N_{\rm H}$, and kT. Within each panel we plot, for our X-ray sources classified as Cyg OB2 members, the difference between the values of the parameter obtained with the two abundance sets as a function of source net counts. The plots are similar to Figure 3 in that the orange crosses indicate, in several observed count ranges, the median and 1σ dispersion of the y-axis values.

We conclude that different choices of abundances make a limited difference for the fit parameters, especially when considering median values. Individual sources, especially low-S/N ones, will end up with somewhat different parameters depending on the adopted abundance sets. We verified, however, that these differences are smaller than the 1σ uncertainties on our best-fit parameters (obtained with the Maggio et al. abundances) in >94% and >98% of the cases, when adopting the SU Aur and V410 Tau abundances, respectively.

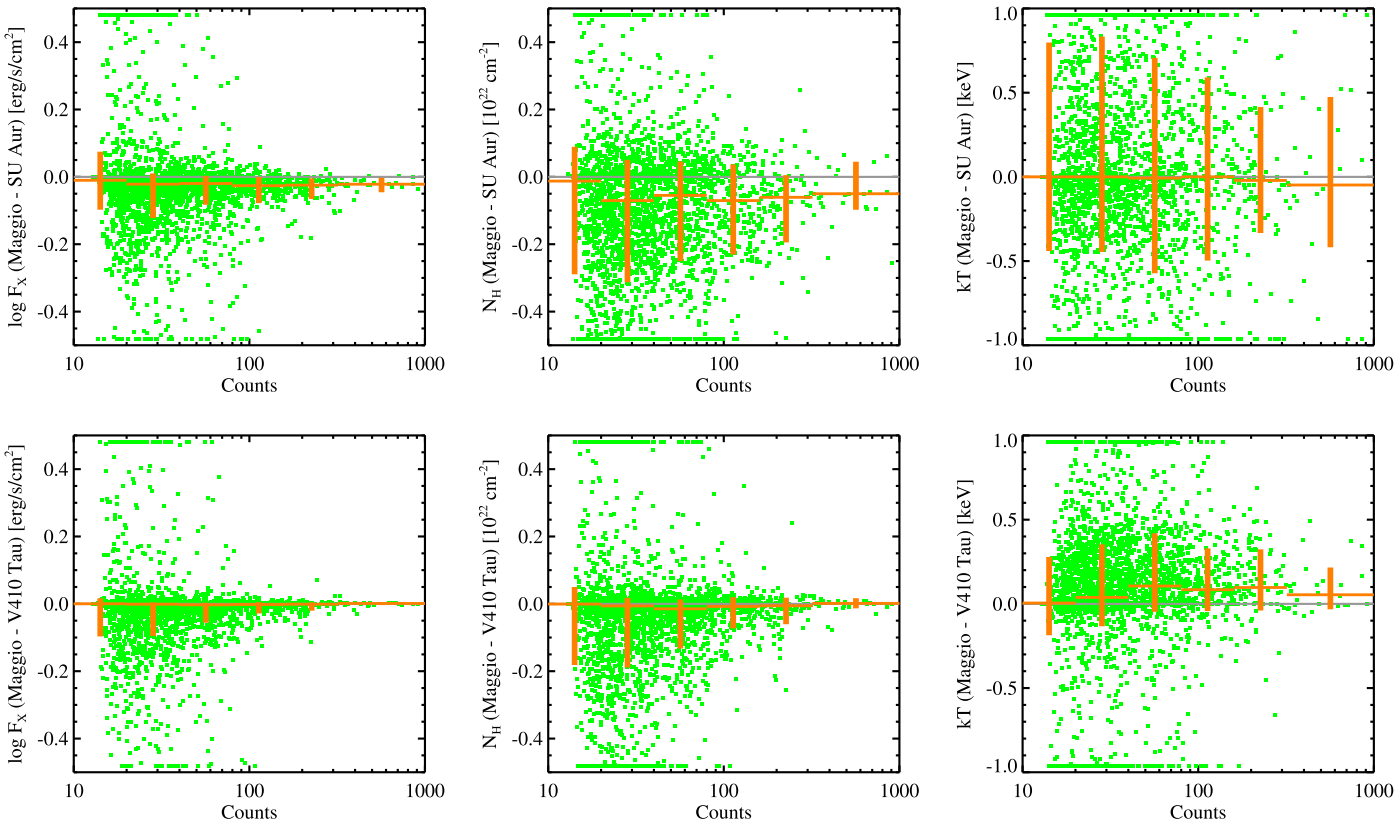

Figure 16. Difference between spectral parameters obtained assuming Maggio et al. (2007) abundances and two significantly different abundance sets derived by Telleschi et al. (2007b) for SU Aur and V410 Tau (top and bottom rows, respectively). Each panel shows, from left to right, the difference in absorption-corrected flux, N_H, and kT, as a function of net detected counts. Green circles refer to individual Cyg OB2 members (with extreme values plotted close to the top and bottom axes), while orange crosses indicate the median and 1σ dispersion of the y-axis values in several count ranges.

ORCID iDs

E. Flaccomio https://orcid.org/0000-0002-3638-5788
J. F. Albacete-Colombo https://orcid.org/0000-0001-8398-0515
J. J. Drake https://orcid.org/0000-0002-0210-2276
M. G. Guarcello https://orcid.org/0000-0002-3010-2310
V. Kashyap https://orcid.org/0000-0002-3869-7996
N. J. Wright https://orcid.org/0000-0002-8389-8711
M. McCollough https://orcid.org/0000-0002-8384-3374
S. Sciortino https://orcid.org/0000-0001-8691-1443

References

Albacete-Colombo, J. F., Flaccomio, E., Drake, J. J., et al. 2023, ApJS, 269, 11
Albacete Colombo, J. F., Flaccomio, E., Micela, G., Sciortino, S., & Damiani, F. 2007, A&A, 464, 211
Anders, E., & Grevesse, N. 1989, GeCoA, 53, 197
Arnaud, K. A. 1996, in ASP Conf. Ser. 101, Astronomical Data Analysis Software and Systems V, ed. G. H. Jacoby & J. Barnes (San Francisco, CA: ASP), 17
Brinkman, A. C., Behar, E., Güdel, M., et al. 2001, A&A, 365, L324
Broos, P. S., Townsley, L. K., Feigelson, E. D., et al. 2010, ApJ, 714, 1582
Cash, W. 1979, ApJ, 228, 939
Comerón, F., Pasquali, A., Rodighiero, G., et al. 2002, A&A, 389, 874
Da Rio, N., Robberto, M., Soderblom, D. R., et al. 2010, ApJ, 722, 1092
Drake, J. J. 2002, in ASP Conf. Ser. 277, Stellar Coronae in the Chandra and XMM-NEWTON Era, ed. F. Favata & J. J. Drake (San Francisco, CA: ASP), 75
Drake, J. J. 2003, AdSpR, 32, 945
Drake, J. J., Brickhouse, N. S., Kashyap, V., et al. 2001, ApJL, 548, L81
Drake, J. J., Laming, J. M., & Widing, K. G. 1996, in IAU Colloq. 152: Astrophysics in the Extreme Ultraviolet, ed. S. Bowyer & R. F. Malina (Dordrecht: Kluwer Academic), 97
Drew, J. E., Greimel, R., Irwin, M. J., & Sale, S. E. 2008, MNRAS, 386, 1761
Feigelson, E. D., Getman, K., Townsley, L., et al. 2005, ApJS, 160, 379
Feldmeier, A., Puls, J., & Pauldrach, A. W. A. 1997, A&A, 322, 878
Fitzpatrick, E. L., & Massa, D. 2007, ApJ, 663, 320
Fruscione, A., McDowell, J. C., Allen, G. E., et al. 2006, Proc. SPIE, 6270, 62701V
Fukugita, M., Ichikawa, T., Gunn, J. E., et al. 1996, AJ, 111, 1748
Getman, K. V., Broos, P. S., Feigelson, E. D., et al. 2011, ApJS, 194, 3
Getman, K. V., Flaccomio, E., Broos, P. S., et al. 2005, ApJS, 160, 319
Gottschalk, M., Kothes, R., Matthews, H. E., Landecker, T. L., & Dent, W. R. F. 2012, A&A, 541, A79
Guarcello, M. G., Drake, J. J., Wright, N. J., et al. 2013, ApJ, 773, 135
Guarcello, M. G., Drake, J. J., Wright, N. J., et al. 2023a, ApJS, 269, 13
Guarcello, M. G., Drake, J. J., Wright, N. J., et al. 2023b, ApJS, 269, 9
Güdel, M., Skinner, S. L., Mel'Nikov, S. Y., et al. 2007, A&A, 468, 529
Hanson, M. M. 2003, ApJ, 597, 957
Hasenberger, B., Forbrich, J., Alves, J., et al. 2016, A&A, 593, A7
Hillenbrand, L. A. 1997, AJ, 113, 1733
Hong, J., Schlegel, E. M., & Grindlay, J. E. 2004, ApJ, 614, 508
Johnstone, C. P., & Güdel, M. 2015, A&A, 578, A129
Jones, A. P. 2004, in ASP Conf. Ser. 309, Astrophysics of Dust, ed. A. N. Witt, G. C. Clayton, & B. T. Draine (San Francisco, CA: ASP), 347
Kashyap, V., Guarcello, M. G., Wright, N. J., et al. 2023, ApJS, 269, 10
Kiminki, D. C., & Kobulnicky, H. A. 2012, ApJ, 751, 4
Kiminki, D. C., Kobulnicky, H. A., Kinemuchi, K., et al. 2007, ApJ, 664, 1102
Laming, J. M. 2009, ApJ, 695, 954
Laming, J. M. 2015, LRSP, 12, 2
Laming, J. M., Drake, J. J., & Widing, K. G. 1995, ApJ, 443, 416
Maggio, A., Flaccomio, E., Favata, F., et al. 2007, ApJ, 660, 1462
Massey, P., & Thompson, A. B. 1991, AJ, 101, 1408
Peres, G., Orlando, S., & Reale, F. 2004, ApJ, 612, 472
Predehl, P., & Schmitt, J. H. M. M. 1995, A&A, 293, 889
Preibisch, T., Kim, Y.-C., Favata, F., et al. 2005a, ApJS, 160, 401
Preibisch, T., McCaughrean, M. J., Grosso, N., et al. 2005b, ApJS, 160, 582
Rauw, G., Nazé, Y., Wright, N. J., et al. 2015, ApJS, 221, 1
Ryter, C. E. 1996, Ap&SS, 236, 285
Sale, S. E., Drew, J. E., Unruh, Y. C., et al. 2009, MNRAS, 392, 497

Schneider, N., Bontemps, S., Simon, R., et al. 2006, A&A, 458, 855
Schulte, D. H. 1956, ApJ, 124, 530
Skinner, S. L., & Güdel, M. 2017, ApJ, 839, 45
Telleschi, A., Güdel, M., Briggs, K. R., Audard, M., & Palla, F. 2007a, A&A, 468, 425
Telleschi, A., Güdel, M., Briggs, K. R., Audard, M., & Scelsi, L. 2007b, A&A, 468, 443
Vink, J. S., Drew, J. E., Steeghs, D., et al. 2008, MNRAS, 387, 308
Vuong, M. H., Montmerle, T., Grosso, N., et al. 2003, A&A, 408, 581
Wood, B. E., Laming, J. M., Warren, H. P., & Poppenhaeger, K. 2018, ApJ, 862, 66
Wright, N. J., Bouy, H., Drew, J. E., et al. 2016, MNRAS, 460, 2593
Wright, N. J., & Drake, J. J. 2009, ApJS, 184, 84
Wright, N. J., Drake, J. J., Drew, J. E., et al. 2012, ApJL, 746, L21
Wright, N. J., Drake, J. J., Drew, J. E., & Vink, J. S. 2010, ApJ, 713, 871
Wright, N. J., Drake, J. J., Guarcello, M. G., et al. 2023a, ApJS, 269, 7
Wright, N. J., Drake, J. J., Guarcello, M. G., Kashyap, V. L., & Zezas, A. 2023b, ApJS, 269, 8
Wright, N. J., Drew, J. E., & Mohr-Smith, M. 2015b, MNRAS, 449, 741
Wright, N. J., Parker, R. J., Goodwin, S. P., & Drake, J. J. 2014b, MNRAS, 438, 639
Zhu, H., Tian, W., Li, A., & Zhang, M. 2017, MNRAS, 471, 3494